

Multimodal laminar characterization of visual areas along the cortical hierarchy

Alessandra Pizzuti^{1,2*}, Pierre-Louis Bazin^{3Ω}, Dimo Ivanov¹,
Sebastian Dresbach^{1,4}, Judith Peters¹, Rainer Goebel^{1,2}, Omer Faruk Gulban^{1,2Ω}

¹Department of Cognitive Neuroscience, Faculty of Psychology and Neuroscience, Maastricht University, Maastricht, NL

²Brain Innovation B.V., Maastricht, NL ³Full brain picture Analytics, Leiden, NL

⁴Department of Neurophysics, Max Planck Institute for Human Cognitive and Brain Sciences, Leipzig, DE

Ω Equal Contribution

*Correspondence: a.pizzuti@maastrichtuniversity.nl

November 18, 2024

Keywords: cortical layers, 7T, microscopy, qMRI, R_2^* , vision

Highlights:

1. We present a multimodal analysis of the laminar organization of four visual regions (V1, V2, V3, hMT+), characterizing progressive visual hierarchy levels in humans. This analysis spans from post-mortem microscopy and quantitative MRI (qMRI) to in-vivo qMRI and laminar fMRI during resting state.
2. Among the three microscopy contrasts, parvalbumin, a marker of interneuron density, emerges as the most distinctive regional feature. Notably, the parvalbumin laminar profiles vary across hierarchy levels, with hMT+ showing the greatest divergence compared to V1, V2, and V3.
3. Quantitative R_2^* (qR_2^*) measurements, from both post-mortem and in-vivo data, reveal a clear increase towards the superficial cortical layers. These depth-dependent patterns closely mirror the laminar profiles observed in both task and resting-state fMRI.

4. Surprisingly, no substantial difference was observed in laminar R_2^* profiles between post-mortem and in-vivo data across the visual areas.

Abstract: Understanding the relationship between brain structure and function is a central goal in neuroscience. While post-mortem studies using microscopic techniques have provided detailed insights into the brain’s cytoarchitectonic and myeloarchitectonic patterns, linking these structural findings to functional outcomes remains challenging. Magnetic resonance imaging (MRI) has emerged as a powerful non-invasive tool for studying both structure and function, but discrepancies in spatial resolution between structural and functional imaging, especially in layer-fMRI, complicate the interpretation of functional results. In this study, we explore how visual cortical hierarchy relates to microscopic and mesoscopic laminar features. Focusing on visual areas that span progressive hierarchical levels, V1, V2, V3, and hMT+, we apply a multimodal approach combining post-mortem histology, post-mortem and in-vivo quantitative MRI (qMRI), and resting-state layer-fMRI. Using the open-access post-mortem AHEAD dataset, which integrates histological and qMRI contrasts from the same brain samples, we bridge microscopic observations with qMRI data. In parallel, we incorporate high-resolution qR_2^* MRI and resting-state layer-fMRI from the same participant, allowing for a comparative analysis of laminar profiles across cortical depth. For computing laminar profiles, we developed an analysis pipeline that bridges histology images, mesoscopic qMRI, and layer-fMRI. Our findings highlight parvalbumin laminar profiles (reflecting interneuron parvalbumin density) as the most discriminative feature for differentiating brain areas. Additionally, we report laminar quantitative T_2^* ($1/R_2^*$) profiles from post-mortem and in-vivo data, together with T_2^* -weighted resting-state layer-fMRI, all of which exhibit a similar overall shape across modalities. Using our methodological framework, a similar laminar characterization can be extended to study other brain regions. Generative models for layer fMRI will benefit from incorporating these new empirical microstructural (parvalbumin) and physical quantitative (qR_2^*) data, leading to more area-specific and accurate models.

1 Introduction

Understanding the functionality of any physical component fundamentally requires exploring the relationship between its structure and function. This principle is a cornerstone of neuroscience, where one of the field’s enduring goals is to elucidate how brain structure underpins its myriad of functions. Since the early 20th century, scientists have conducted extensive post-mortem studies on the brain’s structure, particularly

49 using microscopic techniques that offer spatial resolution at the micrometer scale. These studies have led
50 to the discovery that the brain’s cortical architecture is not uniform. Different brain regions exhibit distinct
51 laminar cytoarchitectonic and myeloarchitectonic patterns, allowing for the establishment of cortical
52 parcellations over time (Brodmann, 1909; Nieuwenhuys, 2013; Vogt, 1906; Zilles and Amunts, 2010).
53 Despite the valuable insights gained from these studies, post-mortem approaches have inherent limitations
54 in capturing functional coupling of microstructures, as functional testing is typically not conducted on the
55 same data sample. Although recent studies have demonstrated the feasibility of combining in-vivo and
56 ex-vivo data from the same participants (Boon et al., 2019; Jonkman et al., 2019), this approach remains
57 challenging and is not yet widely adopted (Fischl and Sereno, 2018).

58 One candidate technique to complement post-mortem brain imaging is magnetic resonance imaging (MRI)
59 as a non-invasive method for studying both brain structure and function (Bandettini et al., 1992; Ogawa
60 et al., 1992). Recently, advancements in ultra high magnetic fields (Koopmans and Yacoub, 2019; Shmuel
61 et al., 2007; Uğurbil et al., 2003; Uludağ et al., 2009) have enabled significant improvements in spatial
62 resolution, allowing for the imaging of the cortical landscape at the mesoscopic scale (< 1 mm). While
63 in-vivo structural imaging could reach a spatial resolution of ≤ 0.35 iso. mm (Bollmann et al., 2022;
64 Gulban et al., 2022; Lüsebrink et al., 2021), the upcoming ‘layer-fMRI field’ for functional imaging has
65 reached submillimeter resolution and aims to test functional hypotheses related to areal microcircuits in
66 vivo (De Martino et al., 2018; Dresbach et al., 2024a; Huber et al., 2017; Petro and Muckli, 2017; Pizzuti
67 et al., 2023; Viessmann and Polimeni, 2021). Despite the push for a higher spatial resolution (below 0.5
68 iso. mm) (Feinberg et al., 2023; Vizioli et al., 2021), currently, the routinely used functional resolution
69 is 0.8 mm isotropic. This discrepancy in resolution between structural and functional scans, leads to
70 new challenges in interpreting the current layer-fMRI results. A potential solution to these challenges is
71 the integration of multiple modalities. For the question of brain parcellation, combining microstructural
72 post-mortem data with topographical and functional in-vivo datasets has resulted in the development
73 of a new multimodal parcellation of the human cerebral cortex (Glasser et al., 2016). This approach
74 has become the consensus standard for fMRI studies. Similarly, quantitative MRI (qMRI) techniques,
75 combined with modeling approaches, provide critical microstructural information to complement in-vivo
76 imaging (Dinse et al., 2015; Trampel et al., 2019; Weiskopf et al., 2021). Notably, among qMRI data,
77 R_2^* ($R_2^* = 1/T_2^*$) relaxation rate serves as a key measurement in understanding tissue microstructure,
78 reflecting changes in magnetic susceptibility that can inform us about iron and myelin deposition. This is
79 particularly relevant in fMRI, where the BOLD signal is predominantly R_2^* -weighted, making R_2^* a key
80 bridge between microstructural properties and functional imaging results. Here, we propose a multimodal
81 study that aims to explore how cortical visual hierarchy relates to microscopic and mesoscopic laminar
82 features. We provide a comprehensive laminar characterization of four visual areas that span progressive

hierarchical levels such as V1, V2, V3 and hMT+. We combined post-mortem histological and qMRI data with in-vivo high-resolution quantitative and resting-state layer-fMRI (rs-fMRI). For the first part, we used the recently published open access post-mortem AHEAD dataset (Alkemade et al., 2022). This dataset includes multiple histological contrasts and three qMRI contrasts from the same brain, providing a unique opportunity to bridge MRI with direct microscopic observations. For the second part, we complement this post-mortem dataset with our in-vivo dataset combining high-resolution qR_2^* MRI at 0.35 iso. mm resolution with resting-state layer-fMRI at 0.8 iso. mm from the same participant. By comparing laminar profiles from the two datasets, we provide a unified perspective on the laminar organization of these visual areas. Among the three microscopy contrasts, parvalbumin (marker of interneurons density) emerges as the most distinctive regional feature that varies across hierarchical levels. Notably, hMT+ parvalbumin laminar profile mostly differs from V1, V2, and V3. Moreover, we provide quantitative laminar profiles of R_2^* for both post-mortem and in-vivo brain samples. Our laminar quantification on microstructural composition and physical R_2^* can be integrated in generative laminar fMRI models (Havlicek and Uludağ, 2020) to improve the areal laminar predictions and the interpretability of layer-fMRI results. Finally, we developed, streamlined and shared all the analysis methods used in this paper to cover the three modalities (histology, qMRI, layer-fMRI) together with our MRI/fMRI dataset. This framework of analysis offers a versatile approach that can be extended to investigate different brain areas, providing the tools to enhance our understanding of structure to function coupling across the entire cortex.

2 Materials and methods

2.1 Data overview

Our data set includes two main sources: the post-mortem 3D whole brain microscopy and 7T quantitative MRI (qMRI) from AHEAD dataset and an in-vivo whole-brain qMRI (R_2^*) at 0.35 iso. mm resolution and resting state fMRI at 0.8 iso. mm from the same participant. A data overview is illustrated in (**Figure 1**).

The post-mortem AHEAD dataset is the first publicly available dataset containing a 3D whole-brain map of multiple microscopy contrasts and 7T qMRI from two human specimens. Whole-brain MRI acquired before sectioning consists of proton density, R_1 and R_2^* MRI maps with an isotropic resolution of 0.4 mm (**Figure 1C**). Coronal slices with in plane resolution of 0.021 mm and 0.20 mm across slices were stained for five microscopy contrasts in an interleaved fashion: two histology stains - Nissl (Thionin, glial and neuronal cell body density) and silver stain (Bielschowsky, fiber density) - and three immunochemistry stains -calbindin, calretinin, parvalbumin (interneurons density). Example slices at original resolution are

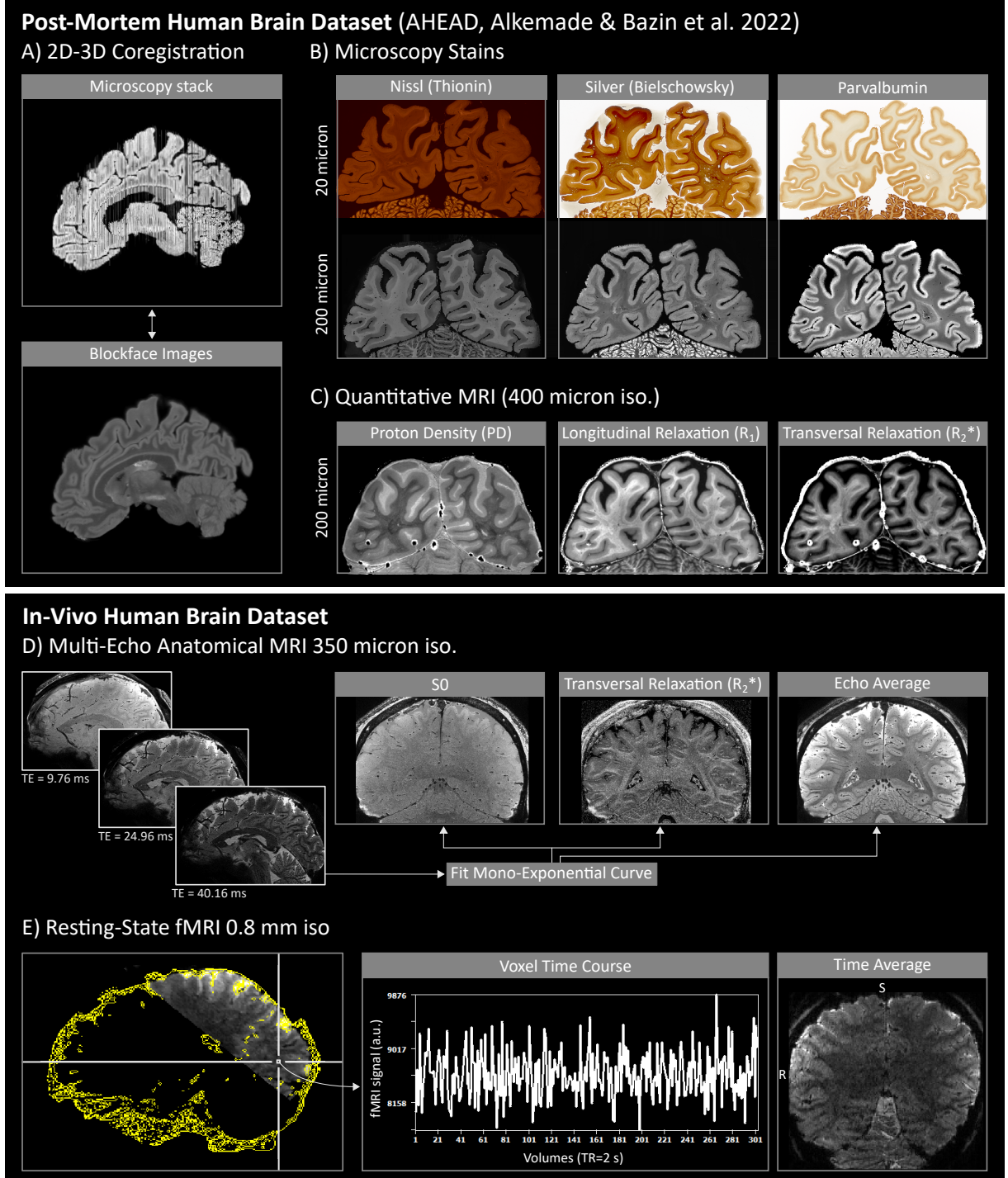


Figure 1: Data overview. A-C) Post-mortem human brain AHEAD dataset consisting of three microscopy stains: Nissl (Thionin) as neural density, Silver (Bielschowsky) as fiber density and Parvalbumin as interneurons density correlate (B) and three qMRI contrasts: proton density (PD), longitudinal relaxation (R_1) and transversal relaxation (R_2^*) (C). Original stains were collected at 20 micrometers, while qMRI were collected at 400 micrometers. Both modalities were co-registered in the same brain space at $150 \times 150 \times 200$ micrometer resolution through 2D-3D registration techniques with respect to the blockface images (A). In-vivo human brain dataset consisting of four runs of whole brain multi-echo multi-shot anatomical MRI at 350 micrometer isotropic resolution (D) and resting-state fMRI data at 0.8 mm isotropic with occipital coverage (E). Three echoes were collected and used to fit a mono-exponential curve and compute S_0 and R_2^* (D). rs-fMRI brain coverage and a voxel time course is shown in panel (E). Co-registration between anatomical and fMRI data was performed between the average echoes and average time course images.

113 shown in **(Figure 1B)**. Note that calbindin and calretinin were only available at the medial part (central)
 114 of the brain, not covering the visual areas of interest. Notably, the authors used advanced post-processing
 115 techniques to align the coronal slices and reconstruct a 3D multi-contrast staining map aligned to the
 116 qMRI maps. As a result, the microscopic underpinning of MRI slices can be studied through the direct
 117 link between microscopy and MRI data. For a comprehensive and detailed description of post-mortem
 118 data collection and reconstruction of AHEAD dataset please refer to the original paper from (Alkemade
 119 et al., 2022). The in-vivo whole brain anatomical R_2^* images and resting-state BOLD fMRI data were
 120 collected from the same participant with the whole-body MAGNETOM 7T “Plus” (Siemens Healthineers,
 121 Erlangen, Germany) at Scannexus B.V. (Maastricht, The Netherlands) using a 32-channel RX head-coil
 122 (Nova Medical, Wilmington, MA, USA). The shimming procedure included the vendor-provided routines
 123 to maximize the field homogeneity within the imaging slab. Anatomical images were collected at 0.35 iso
 124 mm resolution using a newly developed multi-echo multi-shot gradient recalled echo sequence with 3D
 125 echo planar imaging (EPI) readout (Gulban, 2024) **(Figure 1D)**. By combining the strength of a 3D
 126 acquisition and highly segmented k-space through a multi-shot technique, we could collect 0.35 iso. mm
 127 whole-brain anatomical images with very limited geometric distortions in less than 10 min acquisition time
 128 (6 min 48 s). We used a multi-echo 3D EPI sequence (3 echoes), hereby referred to as 3D ME EPI, with
 129 the following main parameters: field of view (FoV) = 200x200x130 mm; orientation = sagittal; bandwidth
 130 = 546 Hz/Px; repetition time (TR) = 52.8 ms; vol.TR = 396 s; echo time (TE) = [9.76, 24.96, 40.16]
 131 ms; flip angle (FA) = 10°; Dual polarity = on; phase partial fourier = off; Segmentation = 40; EPI factor
 132 = 5; PAT mode=CAIPIRINHA; Acceleration factor phase encoding (PE)x3D=3x2; CAIPI trajectory
 133 = w/o z-blips. The complete protocol and the data used in this manuscript are publicly available in
 134 Zenodo: <https://doi.org/10.5281/zenodo.14147820>. We collected a total of four runs. We also used
 135 an available MP2RAGE at 0.35 mm isotropic previously collected in a separate session as “slab-stitched
 136 MP2RAGE” (Gulban, 2024). Briefly, five partial brain slabs at 0.35 iso. mm were concatenated to
 137 achieve whole-brain coverage. Each slab was collected within a single 10 minute run. The slabs were
 138 stitched in a post-processing step to have whole-brain images. Resting-state fMRI data (rs-fMRI) were
 139 collected by using a 2D GE EPI sequence with blood oxygen level dependent (BOLD) contrast (based
 140 on (Moeller et al., 2010)) with 0.8 isotropic mm resolution and coverage of the visual areas of interest
 141 **(Figure 1E)**. The in-plane field of view was 140 × 137 mm (176 × 172 matrix) for a total of 58 acquired
 142 slices. The imaging parameters were: TE = 24.6 ms, TR = 2000 ms, flip angle FA = 69°, in plane
 143 partial Fourier factor 6/8, GRAPPA=3, multi-band (MB)=2. The raw data and the scanning protocol are
 144 available in Zenodo: <https://doi.org/10.5281/zenodo.14164885>. We placed a small functional imaging
 145 slab according to a predetermined positioning based on results from a functional visual localizer obtained
 146 in an independent experimental session (Pizzuti et al., 2024) using the auto-align sequence (AAScout)
 147 from Siemens. Before the acquisition of the main run, we collected 10 volumes for distortion correction

with the settings specified above but opposite phase encoding direction (posterior-anterior). A total of 300 volumes were collected in 10 minutes while the participant was asked to fixate a black fixation cross on a gray background. A frosted screen (distance from eye to screen: 99 cm; image width: 28 cm; image height: 17.5 cm) at the rear of the magnet was used to project the visual stimuli (fixation cross) (using Panasonic projector 28 PT-EZ570; Newark, NJ, USA; resolution 1920x1200; nominal refresh rate: 60 Hz) that participants can watch through a tilted mirror attached to the head coil.

2.2 Region of interest definition and cortical segmentation

We focused our laminar analysis on the following visual areas: V1, V2, V3, and hMT+. The same Region-of-Interest (ROI) definition procedure was applied to both post-mortem and in-vivo dataset. For early visual areas (V1, V2, V3) we coregistered our data to a visual probabilistic functional atlas (visfatlas) (Rosenke et al., 2021) using cortex-based alignment as implemented in BrainVoyager (Goebel, 2012). For hMT+ we used the atlas published by Huang et al., 2019 since hMT+ was only partially included in the visfatlas (one hemisphere was missing in the current release). A schematic illustration of our ROI definition is reported in **Figure 2A** and in **Supplementary Figure 2**. By using visfatlas, we aimed to include the extent of the visual ROIs that can feasibly be stimulated during an fMRI, due to the reduced visual field that can be presented as stimulus in the scanner. For the AHEAD dataset, we used the 'blockface' images to which both microscopy and qMRI maps were aligned to (**Figure 1A**). Blockface images were obtained during sectioning and reconstructed as 3D volume at 0.15 x 0.15 x 0.2 mm resolution. In order to correctly import the post-mortem blockface images into BrainVoyager, we first make isotropic voxels (0.2 iso. mm) and then inverted the contrast. Within BrainVoyager, we downsampled the spatial resolution to 0.5 iso. mm and aligned to the ACPC space. For the in-vivo dataset, we used UNI contrast images from MP2RAGE at original resolution of 0.35 iso. mm coregisted to 3D ME EPI and to fMRI data. We followed Brainvoyager's 'Advanced Segmentation Pipeline' to compute white and gray matter tissue segmentation. A manual refinement of the white matter segmentation was performed by the author A.P. in order to remove the mislabeled voxels creating holes or false geometries, especially around the occipital pole (e.g. around the sinus, subcortical areas). The resulting segmentation files (one from blockfase images and the one from MP2RAGE images) are then used to reconstruct the white matter surfaces within BrainVoyager. On each surface, we defined hMT+ by manual drawing and by matching the characteristic macro-anatomical features reported by Huang and colleagues (e.g. cortical localization, cortical surface areas) (**Figure 2A, Supplementary Figure 2**). The white matter surface was used as input for the cortex-based alignment pipeline of BrainVoyager. Once the alignment to the visfatlas was successfully performed, the ROIs on the cortical surface were all mapped back into the volume space

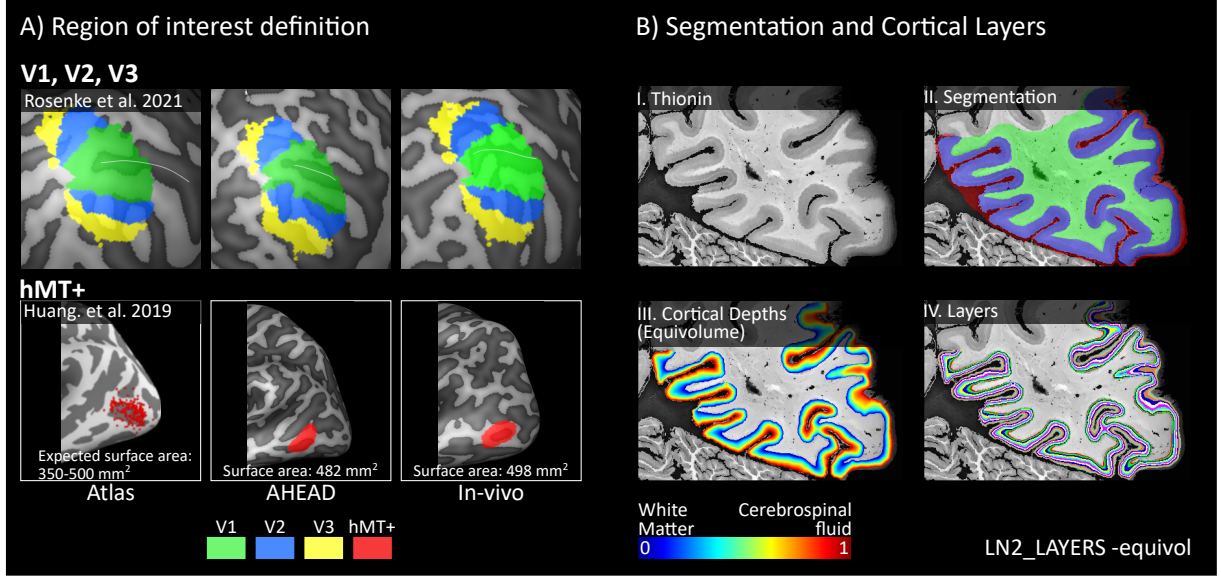


Figure 2: Overview of the two methodological steps. Panel (A) schematically illustrates the procedure used to define the regions of interest. A cortex-based alignment to the functional visual atlas (visfatlas, Rosenke et al. 2021) was used to define V1, V2, V3, while a macroanatomical procedure guided the definition of hMT+ to match a probabilistic atlas (Huang et al. 2019). Please, inspect **Supplementary Figure 2** for an extended overview of our ROI definition. Panel (B) illustrates an example of input (i) for the computation of the geometric cortical layers using the program LN2_LAYERS with the -equivol option. As output, normalized equivolume cortical depth measure (iii) is discretized in 11 equivolume layers (iv). Note that 11 layers are chosen here as an example for visualizing discrete layers; for the main results, the entire cortical depth (iii) is used to compute layer profiles as 2D histograms.

(depth sampling -1 to +3 mm) within BrainVoyager and exported as NIFTI. We projected back into the original resolution 0.15 × 0.15 × 0.2 mm (for AHEAD dataset) and 0.175 iso. mm (for in-vivo dataset) using the program -greedy with 'LABEL' interpolation option to preserve the binary nature of the data (Tustison et al., 2010). The final resolution for in-vivo data (0.175 iso. mm) was chosen to match the resolution of computed R_2^* map (see In vivo MRI and fMRI signal extraction paragraph). Finally, a careful manual tissue segmentation around ROIs in the same native space was performed by A.P. and independently reviewed by O.F.G by using ITK-SNAP software (Tustison et al., 2010). Manual edits were lastly polished by using LN2_RIM_POLISH from LayNii (Huber et al., 2021) that implements a smoothing procedure using a combination of morphological operations of dilation and erosion. An exemplary slice showing the quality of our segmentation is reported in **Figure 2B, ii**. Within the final gray matter space, we projected the ROIs using LN2_VORONOI from LayNii.

2.3 Geometric cortical layers

The definition of cortical depth measures for both post-mortem (at 0.2 iso. mm, nominal) and in-vivo dataset (0.175 iso. mm, nominal) is based on the accurate tissue segmentation (**Figure 2, B (ii)**)

and was performed within LayNii using the LN2_LAYERS -equivol program. This program attributes a normalized (0-1) cortical depth measure to each voxel in 3D according to the equivolume principle (**Figure 2, B (iii)**). Only in the post-mortem data, we ran the algorithm iteratively on each 2D slice (0.15×0.15 mm), since the 3D reconstruction inevitably comes with misalignments and geometrical deformation. We are aware that the equivolume principle is defined for 3D data, however we qualitatively assessed that the amount of errors rising by using a slice-by-slice approach was less compared by using the 3D reconstructed data. Note that, most of the computational mistakes from the slice-by-slice layering procedure were automatically excluded from further analysis due to the 'cutting angle' filtering approach (see AHEAD laminar signal extraction paragraph). Laminar profiles were computed and shown as 2D histograms. The number of bins along the two dimensions (x-as cortical depth and y-as voxel intensity) was adjusted according to the region and the contrast represented. For each 2D histogram, we binned the cortical depth with 21 equivolume layers and overlaid a 'median' laminar profile by computing the median intensity values across voxels belonging to each layer separately. Median was chosen over mean as it is more resilient to outliers that mostly affect tissue boundaries.

2.4 AHEAD volumetric cortical parametrization

The tissue segmentation (**Figure 2, B (ii)**) is also used to define a 3D geodesic coordinate system for each cortical region of interest. This parametrization is needed to run our novel geodesic filters (see Tears filter and Bias Field filter described in AHEAD laminar signal extraction paragraph) for extracting laminar finescale details in AHEAD data. We obtained the first two sets of geodesic coordinates (U,V coordinates) for the gray matter of ROI separately, by running LN2_MULTILATERATE (input: segmentation file). The third coordinate (coordinate D), parametrizing the cortical depth dimension, was computed by running LN2_LAYERS -equivol for each slice of each ROI (input: segmentation file). While we ran the first program using the ROI segmentation computed on the 3D reconstructed model (see 'ROI definition and cortical segmentation' paragraph), the second program was run iteratively for each 2D slice using the final segmentation refined for each slice. In order to preserve the two-dimensional nature of our data, we run our filters on each slice separately by only using 2 instead of 3 coordinates, by setting one of the two (U,V) coordinates to a constant value (e.g. $V=1$). For an extensive explanation on how the coordinates are computed, see Gulban et al., 2022. Although this approach for a volumetric parametrization of the cortex has been previously used in some recent layer-fMRI papers to investigate mesoscopic spatial features (Dresbach et al., 2024a, 2024b; Pizzuti et al., 2023, 2024), we extended it to microscopy data for the first time.

2.5 AHEAD laminar signal extraction

We selected one specimen from AHEAD dataset (ID: 122017) for the highest signal and reduced artifacts in the occipital part of the brain. This specimen had already been reconstructed and aligned with the respective qMRI data at nominal resolution of $0.15 \times 0.15 \times 0.2$ mm by original authors (Alkemade et al., 2022). For the microscopy part of the dataset, we applied three intensity normalization steps in order to enhance fine scale details and remove residual acquisition artifacts within the cortical landscape in the 2D microscopy slices. First, we performed a slice-by-slice intensity normalization based on percentile computation: for each voxel, we subtract the 5th percentile and divide by the difference between 95th and 5th percentile (**Supplementary Figure 1**). In this way, the intensity range is uniform across slices and it is normalized between 0-1. Second, we ran a geodesic low-pass filter with cylindrical kernel (radius: 0.5 and height: 10% of the local cortical depth measurement) by using LN2_UVD_FILTER -median within LayNii for removing high-frequency artifacts (e.g. tears, cracks), that we called 'Tears Filter'. **Figure 3** shows three examples of how the filter mitigates the presence of the artifacts, which are irreversible distortions in the histology field that are induced by cutting, mounting and staining (Fischl and Sereno, 2018, Chapter 4). Finally, we estimated local field bias around each voxel by using the same LayNii program (LN2_UVD_FILTER -median) but with a cylindrical kernel with a larger volume (radius: 0.5 and height: 100% of local cortical depth) and mitigated its effect by dividing the voxel intensity by this estimated field. Lastly, we introduced a new filter 'Cutting Angle Filter' for automatically detecting pieces of the gray matter to exclude from our successive laminar analysis that didn't align well with the coronal cutting place (**Figure 4**). This misalignment is due to the fact that the angle of sectioning relative to the local tissue orientation crucially affects the resulting shape of the lamination pattern. To compare various brain areas, cutting sections had to have a consistent orientation relative to the cortical surface. An angle of 90° is considered optimal to extract cross-section information. Already in the early twentieth century, Von Economo and Koskinas were aware of this problem and conducted their seminal staining work by dissecting each gyrus and sulcus perpendicularly to its axis (Fischl and Sereno, 2018, Chapter 2). Following the same rationale, we developed the 'Cutting Angle Filter' as an alternative algorithmic solution. For our filtering procedure, we computed the local tissue orientation by using LN2_LAYERS -streamlines program from LayNii. This program outputs a 4D NIFTI containing a vector map that attributes to each voxel a radial vector connecting inner and outer gray matter surfaces (locally orthogonal to the two surfaces). Since in this case the 3D geometrical nature of the cortex is used to compute the vector map, we input the segmentation computed on the 3D reconstructed model (**Figure 4, A**). Then, we obtained an angular map (scalar) (**Figure 4, D**) by computing the angle between each voxel's local orientation (**Figure 4, B**) and the vector along the cutting place (coronal) (**Figure 4, C**). Finally, we excluded each voxel whose angle exceeds 150° (**Figure 4, E**). According to Schleicher and colleagues

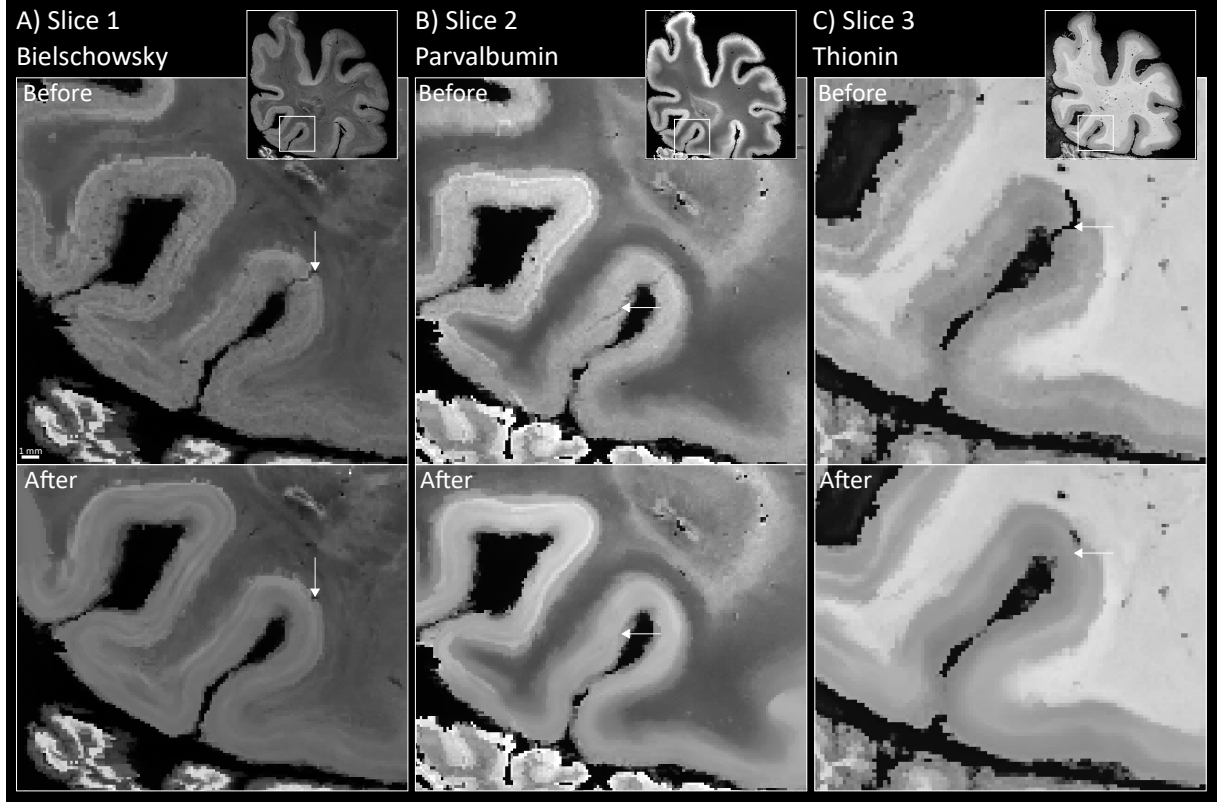


Figure 3: Tears filter. (A-B-C) Three exemplary slices spanning the three microscopy contrasts (Bielschowsky, Parvalbumin, Thionin) showing before and after the application of the tears filter. White arrows pointed to the tears that we aimed to remove. Square inserts showed the entire slices from which we zoomed in to highlight the artifact.

(Schleicher et al., 1999a), a deviation of a maximum 60° from the vertical (90°) was accepted to not alter the laminar pattern. Finally, we quantified the ability of each microscopy contrast (Bielschowsky, Thionin, Parvalbumin) to differentiate visual areas by calculating a measure of similarity as the pairwise correlation between each laminar profile (see **Table 1**). We computed a statistical inference (ANOVA one way) to assess if the correlations across ROIs are different across the three staining contrasts. This was followed by performing a pairwise comparisons post-hoc Wilcoxon signed-rank test. For the qMRI part, the main artifact for the R_2^* map within AHEAD dataset was the presence of vessel residual artifacts that appear as very bright “bubbles” in the data. This is due to the air remaining trapped in the vessels when preparing a post-mortem sample for imaging (Fischl and Sereno, 2018, Chapter 4). We used an intensity-based histogram matching algorithm from ITK-SNAP segmentation tools to detect and exclude affected voxels from further analysis.

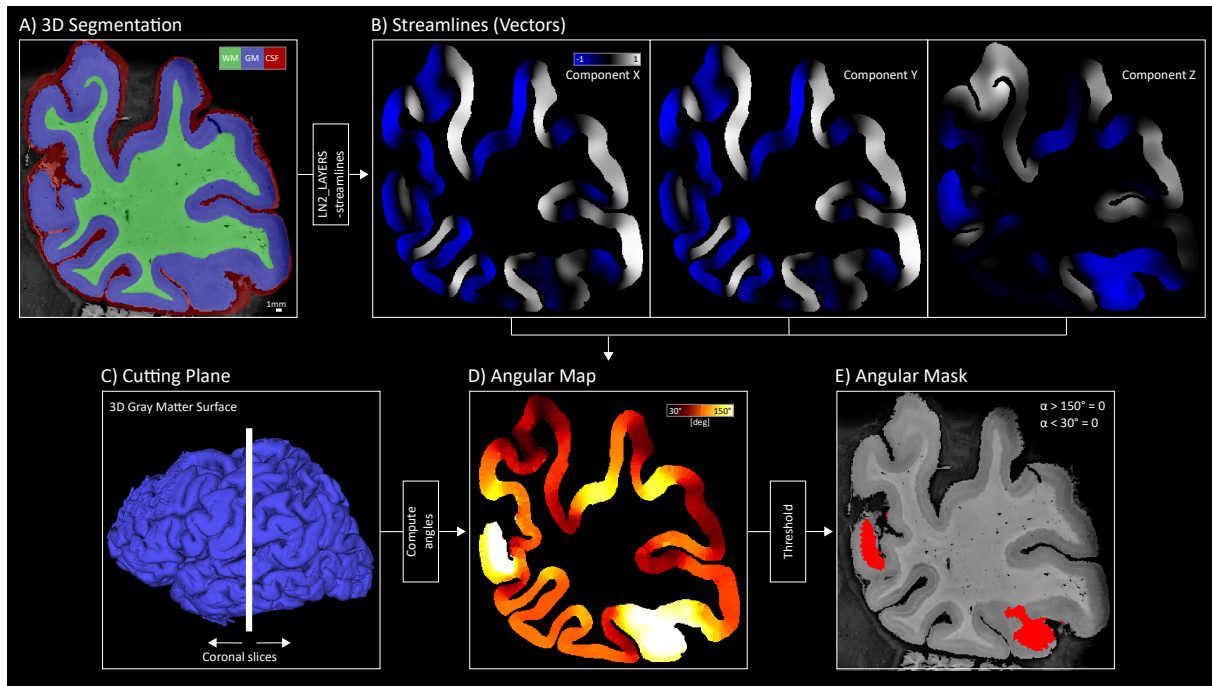


Figure 4: Cutting angle filter steps. A) The 3D segmentation file is used as input for computing the streamlines using the program LN2_LAYERS with -streamlines flag. A tissue segmentation overlaid on a Nissl stained slice is shown as an example. Colors indicate the three tissues, respectively: green for white matter, blue for gray matter and red for cerebrospinal fluid. Note that in post-mortem data the cerebrospinal fluid is physically not present and here indicates the outer boundary of gray matter. B) Streamlines vector field. The three components (x, y, z) of the vector field indicate the local tissue orientation for each voxel are shown for the exemplary slice. C) Schematic visualization of the cutting plane providing coronal slices as a vertical white line overlaid to the gray matter surface. D) The angular map represents the output of the angular computation between streamlines (B) and cutting plane (C). E) A threshold version of the map is shown as an angular mask; red patches indicate excluded areas for an angular measure exceeding 60° with respect to the cutting plane.

2.6 In-vivo MRI and fMRI laminar signal extraction

In order to preserve the fine scale details of our high-resolution 3D ME EPI anatomical images from processing resampling steps, we firstly upsampled each run to double resolution (0.175 iso. mm), as previously done by (Gulban, 2024). We used the `-upsample` function from the `greedy` package with nearest-neighbor interpolation (Yushkevich et al., 2006). For each run separately, we computed the average of the three echos and used them as reference to bring the runs to the same space by using the linear and the non linear registration program from `greedy`. The transformation matrix was then applied to each echo separately. Again, nearest neighbor was used as an interpolation step. Finally, we averaged the four runs and fitted a monoexponential decay function to compute the quantitative R_2^* map. The anatomical images with UNI contrast at 0.35 iso. mm resolution, resulting from slab-stitching procedure, underwent the following processing steps: first, we applied a structure tensor denoising algorithm (Gulban et al., 2018) to increase the SNR (Gulban, 2024). Then, we upsampled to 0.175 iso. mm (as done for ME 3D EPI data) and we registered to the ME 3D EPI space using a non-linear co-registration procedure as implemented in `greedy`. Finally, we resampled our data using linear interpolation and used the resulting output as input to define cortical surfaces, ROIs and tissue segmentations. Resting-state fMRI (rs-fMRI) data at 0.8 iso. mm underwent the following preprocessing steps: slice time correction (BrainVoyager), motion correction (BrainVoyager), distortion correction (FSL TOPUP), high-pass filter with 3 cycles (BrainVoyager). We averaged the time series and upsampled to 0.175 iso. mm to match anatomical resolution using the `ndimage.zoom` command from `scipy` (Virtanen et al., 2020) with spline interpolation (order 3). We coregister rs-fMRI data to high-resolution T_2^* anatomical images (ME 3D EPI space) using a non-linear registration algorithm as implemented in `greedy` with linear interpolation.

2.7 Estimation of scaling factor between post-mortem and in vivo R_2^* laminar profiles

To evaluate the relative contribution of microstructure and vasculature in the resulting R_2^* , as the signal shifts from being influenced solely by microscopic factors (post-mortem) to a combination of microscopic and vascular contributions (in-vivo), we estimated a scaling factor between quantitative R_2^* laminar profiles between the two datasets. While brain fixation has been shown to significantly affect the R_1 range (Dinse et al., 2015), its impact on R_2^* is considered minimal (Deistung et al., 2016). Given the similar R_2^* ranges observed, we attribute the differences between in vivo and post-mortem R_2^* primarily to variations in tissue composition. For each laminar profile (four ROIs, two hemispheres, two datasets), we fit a linear regression model. For each ROI, we averaged the slope between the two hemispheres. Then, we divided

301 the slope fitted on the post-mortem by the slope fitted on the in-vivo data. This ratio estimates the
302 scaling factor of the R_2^* laminar profiles between the two modalities.

303 3 Results

304 3.1 Comparing the microscopic cortical architecture of visual areas

305 We report the lamination patterns of four visual areas, V1, V2, V3, and hMT+, using three microscopy con-
306 trasts: Bielschowsky, Thionin, and Parvalbumin (**Figure 5** and **Supplementary Figure 3**). Bielschowsky
307 staining correlates with fiber density and indirectly with myelin, while Thionin and Parvalbumin provide
308 cellular information by staining neuronal cell bodies and a subset of inhibitory interneurons, respectively.
309 This analysis enables us to characterize each ROI by comparing the expression of these three microscopic
310 features across cortical depths. We quantified the ability of each microscopy contrast to differentiate
311 visual areas by calculating a measure of similarity (indexed as the pairwise correlation between each
312 laminar profile (**Table 1**). Parvalbumin exhibited the lowest level of similarity across regions compared to
313 Bielschowsky and Thionin, which was also qualitatively visible when comparing laminar profiles (**Figure 5**
314 and **Supplementary Figure 3**). To support our comparisons, we tested if the correlations across the
315 three groups are different: a one way ANOVA shows significant differences across groups ($F = 9.03$, $p =$
316 0.0007). A pairwise comparisons using post-hoc Wilcoxon signed-rank test revealed significant difference
317 (after Bonferroni correction) between Parvalbumin and Bielschowsky ($p = 0.002$) and Parvalbumin and
318 Thionin ($p = 0.02$) and not significant between Bielschowsky and Thionin ($p = 0.1$). Unlike cellular
319 neuronal density, the distribution of Parvalbumin neurons varies characteristically across cortical depths
320 and ROIs. The different distribution of parvalbumin neurons across layers may suggest a differential
321 contribution to inhibitory processing with a maximum for intermediate layers.

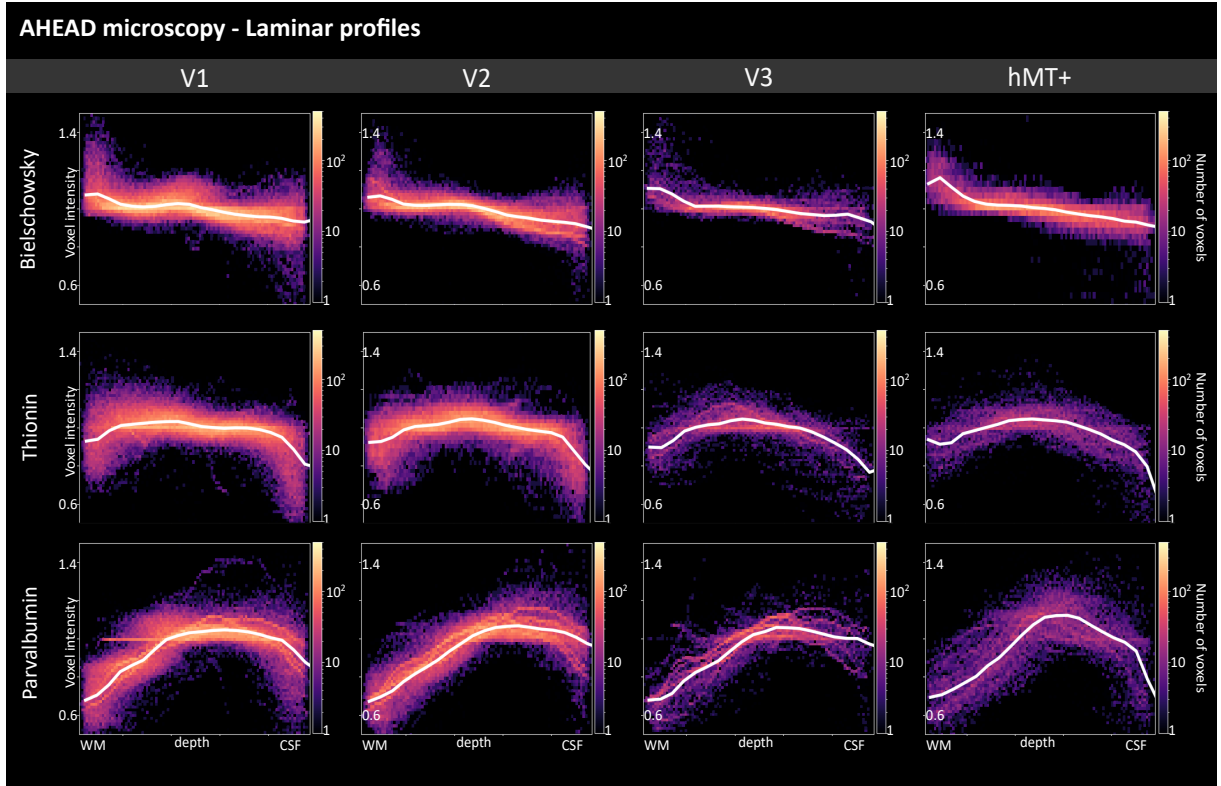
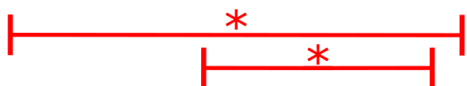


Figure 5: AHEAD laminar profiles for three microscopy contrasts (Bieloschowsky, Thionin, Parvalbumin) are shown as 2D histograms for each ROI of the left hemisphere. Gray matter cortical depth measure is shown from white matter ($x=0$) to cerebro-spinal fluid ($x=1$) boundary from left to right. Solid white lines in each subplot show median intensity for 21 discrete equivolume layers. The Y-axis is shown within the 0.5-1.4 (a.u.) range for each subplot. Results from the right hemisphere are shown in **Supplementary Figure 3**.

Table 1: Similarity of laminar profiles (rho). Correlations are computed to quantify similarity across laminar profiles between each ROI (V1, V2, V3, hMT+) for each microscopy contrast. Low correlation values indicate high dissimilarity between laminar profiles of different regions. Significant differences are found between Parvalbumin and Bielschowsky and Parvalbumin and Thionin and are highlighted by a red asterisk ($p < 0.01$).



| (LH) | Bielschowsky | Thionin | Parvalbumin |
|---------|--------------|---------|-------------|
| V1-V2 | 0,994 | 0,994 | 0,997 |
| V1-V3 | 0,997 | 0,985 | 0,989 |
| V2-V3 | 0,996 | 0,996 | 0,991 |
| V1-hMT+ | 0,993 | 0,961 | 0,942 |
| V2-hMT+ | 0,995 | 0,963 | 0,921 |
| V3-hMT+ | 0,996 | 0,948 | 0,917 |
| (RH) | Bielschowsky | Thionin | Parvalbumin |
| V1-V2 | 0,999 | 0,999 | 0,995 |
| V1-V3 | 0,993 | 0,998 | 0,978 |
| V2-V3 | 0,996 | 0,999 | 0,974 |
| V1-hMT+ | 0,998 | 0,988 | 0,938 |
| V2-hMT+ | 0,998 | 0,989 | 0,925 |
| V3-hMT+ | 0,995 | 0,989 | 0,981 |

3.2 Comparing post-mortem and in-vivo quantitative R_2^* laminar profiles

Bridging the gap between post-mortem and in-vivo studies is crucial for understanding the sources of R_2^* , as it is assumed that the signal shifts from being influenced solely by microscopic factors (post-mortem) to a combination of microscopic and vascular contributions (in-vivo). Therefore, in this study, we report the quantitative R_2^* values across cortical depths for both post-mortem and in-vivo datasets (**Figure 6** and **Supplementary Figure 4**). **Table 2** accompanies **Figure 6** and **Supplementary Figure 4** by reporting the average R_2^* value in only three equivolume layers. First, our R_2^* cortical layer profiles matches with the previously reported R_2^* values within the visual cortex (Gulban et al., 2022). Second, we also observe overall matching profiles between the AHEAD and in-vivo data that shows a consistent decrease of R_2^* values from deep to the superficial layers. When comparing the magnitude of the R_2^* laminar profiles between post-mortem and in-vivo data, we show that the AHEAD R_2^* values are lower compared to those measured in vivo. In addition, the discrepancy between the R_2^* values seem to be the highest in superficial layers. This discrepancy is expected, as in-vivo R_2^* values include the additional contribution from blood vessels, leading to a faster signal decay. In contrast, post-mortem R_2^* is influenced only by iron and myelin content, since the brain fixation process removes most of the blood, resulting in a slower decay. These differences are most pronounced from the middle to the superficial layers, which is expected due to the presence of more vasculature and partly by pial veins (partial volume effect). We estimate an average scaling factor across our visual ROIs between post-mortem and in-vivo of 2.8 (**Table 3**). This means that, the blood affects the estimation of R_2^* with a factor of three: the slope of the R_2^* laminar profiles in vivo are almost three times smaller compared to the one measured when microstructure only is considered (post-mortem).

Table 2: Mean quantitative R_2^* [Hz] reported for three equivolume layers (deep, middle, superficial) for all the regions of interest in both post-mortem and in-vivo data.

| | R2* [Hz] Post-mortem | | | R2* [Hz] In-vivo | | |
|-------------|-----------------------------|---------------|--------------------|-------------------------|---------------|--------------------|
| | Deep | Middle | Superficial | Deep | Middle | Superficial |
| (LH) | | | | | | |
| hMT+ | 30,91 | 26,08 | 16,37 | 33,78 | 30,81 | 27,34 |
| V1 | 30,83 | 26,25 | 18,12 | 33,97 | 32,11 | 29,14 |
| V2 | 34,48 | 29,29 | 19,65 | 34,5 | 31,02 | 28,47 |
| V3 | 33,87 | 29,21 | 18,94 | 32,96 | 29,74 | 28,05 |
| (RH) | | | | | | |
| hMT+ | 32,62 | 27,11 | 17,27 | 34,23 | 31,3 | 26,93 |
| V1 | 34,18 | 28,24 | 19,58 | 32,92 | 31,35 | 29,34 |
| V2 | 37,82 | 31,56 | 20,41 | 34,38 | 31,18 | 28,55 |
| V3 | 38,53 | 20,54 | 17,15 | 33,15 | 29,33 | 27,11 |

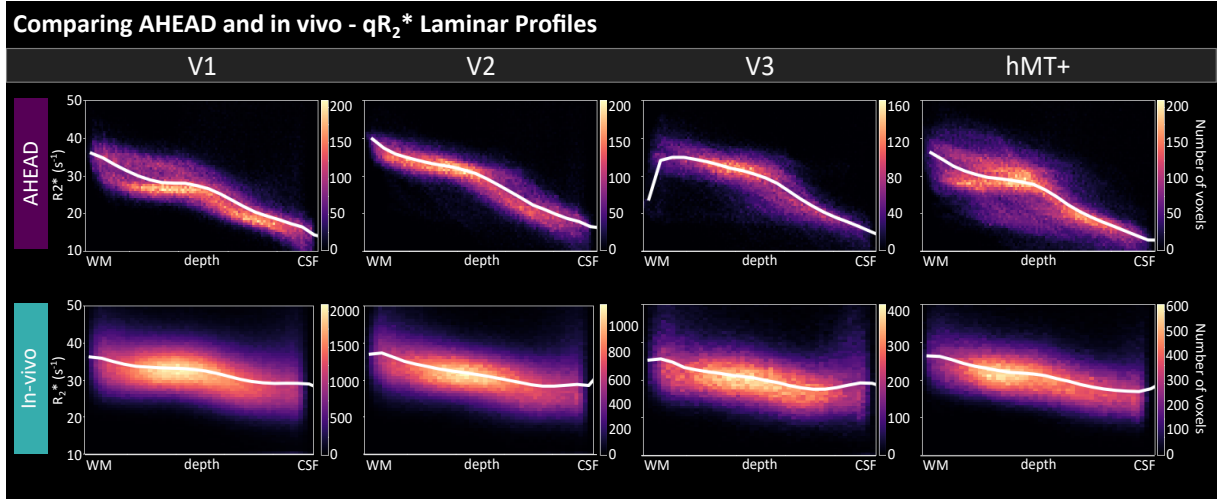


Figure 6: AHEAD (top) and in-vivo (bottom) qR_2^* laminar profiles are shown as 2D histograms for each ROI for the left hemisphere. Gray matter cortical depth measure is shown from white matter ($x=0$) to cerebro-spinal fluid ($x=1$) boundary from left to right. Solid white lines in each subplot show median intensity for 21 discrete equivolume layers. The Y-axis is shown within the 10-50 (s^{-1}) range for each subplot. Results from the right hemisphere are shown in **Supplementary Figure 4**.

Table 3: Regression modeling for R_2^* laminar profiles. The slope of the fitted curve is reported for each ROI. The ratio is considered as an estimate of the scaling factor between the two modalities.

| Post-mortem (slope) | V1 | V2 | V3 | hMT+ |
|-------------------------------------|-----------|-----------|-----------|-------------|
| Left hemisphere | -22,39 | -24,87 | -21,2 | -24,74 |
| Right hemisphere | -24,01 | -28,51 | -34 | -26,33 |
| Average | -23,2 | -26,69 | -27,6 | -25,53 |
| In-vivo (slope) | V1 | V2 | V3 | hMT+ |
| Left hemisphere | -8,48 | -8,91 | -7,95 | -10,01 |
| Right hemisphere | -7,37 | -10,11 | -9,43 | -11,16 |
| Average | -7,92 | -9,51 | -8,9 | -10,55 |
| Ratio: Post-mortem / In-vivo | 3 | 2,8 | 3,1 | 2,4 |

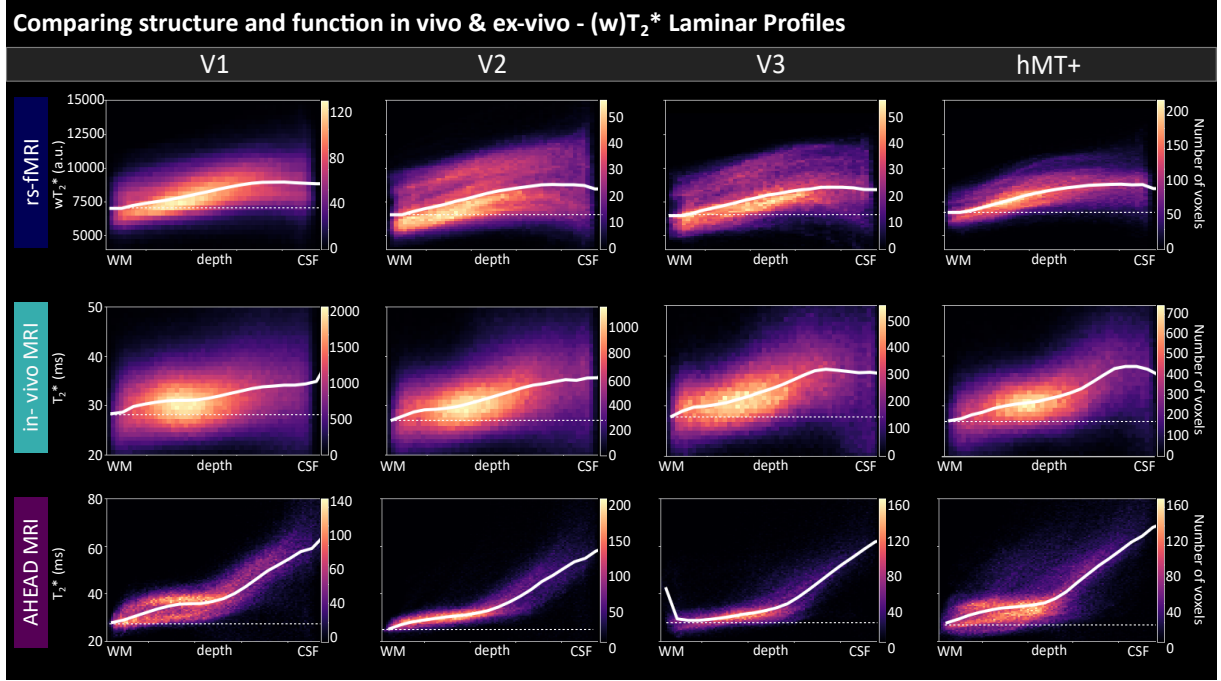


Figure 7: Structure-to-function comparison. Resting-state fMRI (top), in-vivo T_2^* (middle) and post-mortem AHEAD T_2^* (bottom) laminar profiles are shown as 2D histograms for each ROI. Gray matter cortical depth measure is shown from white matter ($x=0$) to cerebro-spinal fluid ($x=1$) boundary from left to right. Solid white lines in each subplot show median intensity for 21 discrete equivolume layers. Dotted lines indicate horizontal lines to highlight the increase towards superficial layers of main curves. The Y-axis range is displayed only in the first subplot of each data type and kept invariant across ROIs. Results from the right hemisphere are shown in **Supplementary Figure 5**.

3.3 Comparing structure to function: anatomical T_2^* and resting state fMRI

Since GE-BOLD fMRI signals reflect variations of T_2^* between conditions, we analyzed both anatomical and functional signal as T_2^* variation ($1/R_2^*$). Here, our goal is to report the laminar profiles from the rs-fMRI run and to compare it to the anatomical T_2^* laminar profiles from both in-vivo and post-mortem AHEAD dataset (**Figure 7** and **Supplementary Figure 5**). In all ROIs, the rs-fMRI signal exhibits a general increase towards the cortical surface, similar to the anatomical profiles in the two datasets. Although at half of the spatial resolution (0.8 iso. mm), the same overall characteristic positive slope laminar feature we observed in the anatomical T_2^* is also present within the rs-fMRI data. However, finer details observable in the anatomical laminar profiles, such as the characteristic dip in T_2^* , remain concealed in the current resting state laminar profiles due to the varying spatial scales. Future fMRI studies employing higher spatial resolution may uncover these details (Feinberg et al., 2023).

4 Discussion

4.1 Summary

In this study, we propose a multimodal laminar characterization for four human visual areas (V1, V2, V3, hMT+) that aims to bridge the micro and mesoscale. We used the novel publicly available post-mortem AHEAD dataset, which uniquely presents multiple microscopy contrasts and quantitative MRI for the same individual, and complement it with our in-vivo dataset consisting of both high-resolution anatomical and functional MRI (**Figure 1**). We investigated the microscopic underpinning of our regions of interests by analyzing the cortical variation of three microscopy contrasts (Bielschowsky, Thionin, Parvalbumin) and found a central role for Parvalbumin for area differentiation (**Figure 5, Supplementary Figure 3**). Moreover, we compared R_2^* MRI cortical variation of post-mortem to in vivo samples, and found a common linear decrease R_2^* across the two modalities (**Figure 6, Supplementary Figure 4**). Finally, we report the laminar profiles in rs-fMRI (**Figure 7, Supplementary Figure 5**) and compare it with the structural laminar profiles measured in the same living brain and in post-mortem brain. Although at different spatial resolution, the same overall characteristic positive slope characterized the three laminar profiles.

4.2 Implications for layer-fMRI

Cortical distribution of Parvalbumin interneurons. It is generally assumed that the neural activity of excitatory neurons is reflected in BOLD fMRI response, since excitatory neurons constitute 80-90% of all cortical neurons (Meyer et al., 2011). However, it is known that the ratio between excitatory and inhibitory neurons varies across cortical depth and areas (Markram et al., 2004; Tremblay et al., 2016). Even though our microscopy data cannot quantify the ratio of excitatory and inhibitory neurons, we still found it notable that the cortical distribution of Parvalbumin neurons is a characteristic feature of the region of interest (**Figure 5**). Parvalbumin neurons, even if they represent only one category of interneurons, they are the most abundant GABAergic neurons in the cortex (Rudy et al., 2011) and are assumed to have indirect influence through the inhibition of pyramidal cells, resulting in vasoconstriction (Lee et al., 2021). Due to this property, neural mechanisms involving this category of interneurons can affect the hemodynamic response detected by fMRI (Moon et al., 2021). In particular, when submillimeter resolution is available for layer-fMRI studies, unveiling the cortical distribution of parvalbumin interneurons can be crucial to interpret the laminar results when an inhibitory circuit is hypothesized to be recruited for solving functional tasks. For instance, (Torres-Gomez et al., 2020) suggested that changes in the

proportion of parvalbumin neurons in layers 2/3 cells may favor the emergence of activity encoding working memory in association areas in primate brains. We expect that integrating a proxy for microstructural neural information in humans will improve the interpretation of laminar functional response in resolving complex tasks.

Vascular vs microstructural gray matter composition. When reaching submillimeter spatial resolution in fMRI, signals from different cortical laminae can be disentangled. However, at this spatial scale also other mesoscopic details regarding the underlying vascular network have to be considered while discussing layer-fMRI results. In particular, the BOLD signal reflects variation of T_2^* mainly coming from veins (Koopmans and Yacoub, 2019; Uludag and Havlicek, 2021). The presence of pial veins together with intracortical veins usually induces a bias known as ‘draining vein’ effect that is manifested as a signal that linearly increases towards the cortical surface. This is due to the fact that the blood is drained from deep to superficial layers by the veins that accumulate signals while traveling upwards, making the identification of the neural laminar source challenging (Koopmans and Yacoub, 2019). This cortical trend has been reported for both task-induced (Aitken et al., 2020; Fracasso et al., 2018; Mourik et al., 2021) and resting-state activity (Guidi et al., 2020; Markuerkiaga et al., 2021; Pais-Roldán et al., 2020). In this study, we showed that a linear trend characterizes the gray matter structure both in-vivo and post-mortem qT_2^* laminar profiles (**Figure 7**). When the vasculature is taken out of the equation, as in the post-mortem case, T_2^* is still the highest at superficial layers. This result suggests that microstructural properties (e.g. myelin, iron) contribute to the linear increase in addition to vasculature in both task and resting state fMRI. Given that regional differences in the relative contributions of microstructure and vasculature are likely, understanding how these elements might consistently or differentially shape T_2^* profiles across brain regions could enhance our interpretation of laminar fMRI. A scenario where both factors together produce a consistent linear increase across the cortex would align with prior observations, underscoring the importance of further investigation. Extending generative laminar models to embed area-specific microstructural and vascular features (such as R_2^* laminar profile) might complement and improve our understanding of the sources of variance driving layer-fMRI (Havlicek and Uludağ, 2020; Markuerkiaga et al., 2016).

Consequences for models of layer fMRI. Generative laminar models are useful tools to predict layer fMRI dynamics. However, the complexity and the accuracy of those models depends on the assumptions and on the physical parameters estimates (Havlicek and Uludağ, 2020; Markuerkiaga et al., 2016; Uludağ et al., 2009). Below, we discuss our resting-state laminar profiles together with the generative laminar model from (Havlicek and Uludağ, 2020). The model uses two compartments (intravascular (blood) and extravascular (parenchyma)) to describe the BOLD signal generated by a GE sequence (Eq. 1, Appendix). T1 effects are neglected in this model. As the signal from the intravascular compartment

can be neglected at 7T (due to R_2^*), the predicted laminar profile depends only on the extravascular compartment. According to this modeling, the variables affecting the signal are:

1. S_0 or ρ , baseline signal intensity measured at $TE=t(0)$, when no relaxation (particularly T_2^* relaxation) has taken place. This signal measures the water proton density in the tissue.
2. CBV, cerebral blood volume, measuring the fraction of cerebral blood volume within a given amount of brain tissue.
3. R_2^* , the transverse relaxation rate, which reflects how quickly the MRI signal decays in a gradient-echo sequence.

Conventionally, it is assumed that both S_0 and R_2^* are constant across cortical layers and only CBV is expected to increase from deep to superficial layers (see Table 2, from Havlicek and Uludağ, 2020). Under this set of assumptions, the equation predicts a signal decreasing from deep to superficial layers (see Appendix - Laminar resting state fMRI). However, our empirical laminar resting-state fMRI profile shows the opposite trend (**Figure 7, Supplementary Figure 5**) with respect to the prediction. A similar trend to our results was also reported in previous works (Guidi et al., 2020; Markuerkiaga et al., 2016; Pais-Roldán et al., 2020). This discordance between modeling and empirical data points to the obvious conclusion that some of the above assumptions have to be relaxed in order to counterbalance the effect of CVB. In this work, we focus on quantitative R_2^* and consistently show in both post-mortem and in-vivo R_2^* is clearly modulated (and not constant) with respect to cortical depth. The laminar variation of R_2^* with its characteristic decrease from deep to superficial layers is one factor that counterbalances the effect of CBV: as R_2^* decreases with cortical depth, the T_2^* weighted rs-fMRI signal increases with cortical depth. Together with R_2^* , it is plausible to think that S_0 also changes across cortical depth as a concurrent contribution to the resulting laminar profile measured during a rest condition. Empirical data, such as our observed laminar profiles, are invaluable in challenging and refining these models, offering insights that purely theoretical approaches may overlook. A full suite of modeling simulations is necessary to systematically explore the combined effects of both R_2^* and S_0 on the laminar profile. This approach can help resolve the observed divergence between current modeling predictions and empirical findings. By adjusting these parameters within the model, future work may better capture the nuanced interactions that shape the laminar BOLD signal across cortical depth, ultimately leading to more accurate representations of layer fMRI dynamics.

4.3 Extending open access tools for the AHEAD dataset

Publicly available post-mortem datasets are invaluable for studying the microscopic structure of the human brain (Alkemade et al., 2022; Amunts et al., 2013). However, developing specialized analysis toolboxes is also essential for correctly extracting information from these rare datasets and integrating it with other modalities. For instance, the Allen Brain Map portal (<https://portal.brain-map.org/overview>) is complemented by a suite of publicly available analysis tools (<https://github.com/AllenInstitute>). Following the same rationale, our streamlined analysis pipeline released as an open github repository (https://github.com/27-apizzuti/multimodal_layers.git), extends the open access analysis tools for the AHEAD dataset provided by Alkemade and colleagues, offering new tools for extracting laminar information. To enhance the laminar details and ensure robust cortical sampling from multiple slices, we developed the ‘cortical tears filter’ (**Figure 3**) and the ‘cutting angle filter’ (**Figure 4**). These tools are crucial for deriving reliable contrast- and ROI-specific laminar information. While we acknowledge the existence of other softwares addressing similar artifacts (Kindle et al., 2011; Mancini et al., 2020; Schleicher et al., 1999b), we highlight that our implementation is designed to encourage widespread use of AHEAD dataset specifically by offering tools that can be applied on the downloaded data. Note that the tissue segmentation step is not fully automated and requires expertise and manual work. This is a crucial step for accurate and precise layer profiles when working with very high resolution images. With all analysis methods and data used in this paper (histology, qMRI, and layer-fMRI) being publicly accessible, our framework offers a valuable resource for researchers conducting similar studies in other brain regions. By facilitating the study of cortical laminar structure and integrating this with functional information, our approach supports a deeper understanding of the structure-function relationships across the cortex, potentially uncovering unique regional patterns that contribute to brain function and disease.

4.4 Limitations and conclusions

Although our efforts to bridge scales and techniques have led to new insights and discussions on the laminar organization of four visual areas, it is worth pointing out the limitations of our results. Firstly, we focused on a limited subset of visual regions (V1, V2, V3, hMT+), which restricts the scope of our findings from drawing widespread conclusions on laminar features and visual hierarchy. Secondly, we defined the ROIs for V1, V2, and V3 using the visfatlas (Rosenke et al., 2021) with cortex-based alignment, and hMT+ was delineated based on macro-anatomical criteria outlined in (Huang et al., 2019). While we acknowledge that different methodologies can lead to partially overlapping regional boundaries (Turner, 2019 and Fischl and Sereno, 2018, Chapter 7), we argue that these discrepancies are unlikely to

478 impact our results as we aim to understand regional and not local lamination differences. Additionally,
 479 comparing post-mortem and in vivo tissue introduces limitations due to the effects of brain extraction
 480 and fixation. These effects could influence the R_2^* measurements (Deistung et al., 2016) and may alter
 481 the apparent thickness of cortical layers due to slight tissue shrinkage during fixation (Mouritzen Dam A.,
 482 1979). Finally, the small sample size, relying on data from only one post-mortem and one in vivo brain,
 483 limits the generalizability of our findings to broader populations, as individual anatomical variations may
 484 not be fully represented. However, the fundamental structural features observed in this study are likely
 485 to be consistent across human brains, supporting the broader relevance of our findings. Therefore, it is
 486 critical that similar post mortem and in vivo high resolution imaging efforts continue in the future where
 487 the amount of publicly available datasets increase. We conclude that our study represents a step forward
 488 along the goal of studying structure to function coupling mechanisms. Our results on regional laminar
 489 differences observed using multi-modal and multi-contrast data opens up new discussions on interpretation
 490 of layer-fMRI data. Future research could focus on expanding the multimodal characterization to include
 491 additional visual areas and functional contexts, enhancing our understanding of the dynamic interplay
 492 between micro- and mesoscale features in visual processing.

493 5 Appendix

494 Laminar resting state fMRI

495 The laminar BOLD signal equation (Eq. 5 from Havlicek and Uludağ, 2020) for a cortical layer (denoted
 496 by subscript k) for a baseline condition (denoted by subscript 0) is given as:

$$S_{0,k} = \left(1 - \sum_i V_{0i,k}\right) S_{0,Ek} + \sum_i V_{0i,k} S_{0,Ik} \quad (1)$$

497 where:

- 498 1. $V_{0i,k}$ is the cerebral blood volume (CBV) from the vascular compartment (denoted by subscript i)
 499 at baseline for the k -layer.
- 500 2. The vascular compartment include the venules and ascending veins compartments.
- 501 3. $S_{0,Ik}$ is the intravascular signal at baseline for the k -layer.

502 Laminar resting state fMRI

503 Under the approximation that, at 7T, R_2^* of the blood (intravascular) is twice as fast as R_2^* of the
 504 parenchyma, we can assume that $S_{\text{rest}0, Ik} = 0$ Havlicek and Uludağ, 2020.

505 Thus, we can write:

$$S_{\text{rest}0, k} = \left(1 - \sum_i V_{0i, k}\right) S_{\text{rest}0, Ek} \quad (1)$$

506 Since the parenchyma R_2^* (extravascular) is assumed to be constant across cortical depth, we approximate
 507 $S_{\text{rest}0, Ek}$ to be constant as well across cortical depth (Havlicek and Uludağ, 2020).

$$S_{\text{rest}0, k} \approx \left(1 - \sum_i V_{0i, k}\right) \quad (2)$$

508 As CBV_0 is expected to linearly increase across cortical depth (Havlicek and Uludağ, 2020), the resulting
 509 signal at resting state is expected to decrease as a function of cortical depth.

510 **6 Data and Software availability statement**

511 Analysis code is available on GitHub: <https://github.com/27-apizzuti/multimodal.layers.git>. Please refer
 512 to Alkemade et al., 2022 for raw post-mortem data. In-vivo anatomical data are shared in Zenodo:
 513 <https://doi.org/10.5281/zenodo.14147820>. Raw resting-state laminar-fMRI data are shared in Zenodo:
 514 <https://doi.org/10.5281/zenodo.14164885>. Preprocessed data from both post-mortem and in-vivo
 515 datasets are shared in Zenodo: <https://doi.org/10.5281/zenodo.14164885>.

516 **7 Acknowledgements**

517 This project was funded by the EU-project H2020-860563 euSNN and the European Union's Horizon 2020
 518 Framework Programme for Research and Innovation under the Specific Grant Agreement No. 945539
 519 (Human Brain Project SGA3). In-vivo data was acquired at Scannexus (Maastricht, the Netherlands).
 520 OFG is funded by Brain Innovation. We thank Kamil Uludag for helpful discussions on the laminar
 521 modeling. SD is supported by the 'Robin Hood' fund of the Faculty of Psychology and Neuroscience and
 522 the department of Cognitive Neuroscience.

7.1 Declaration of interests

The authors declare that they have no known competing financial interests or personal relationships that could have appeared to influence the work reported in this paper.

8 Author Contributions

According to the CRediT system (<https://casrai.org/credit/>)

Conceptualization: A.P., O.F.G., P.B.

Methodology: A.P., O.F.G., P.B.

Software: A.P., O.F.G.

Validation: A.P., O.F.G.

Formal Analysis: A.P.

Investigation: A.P., O.F.G.

Resources: A.P., O.F.G., P.B., J.P., R.G.

Data curation: A.P.

Writing – original draft: A.P.

Writing – review & editing: A.P., P.B., O.F.G., D.I., S.D., J.P., R.G.

Visualization: A.P.

Supervision: O.F.G., P.B.

Project administration: O.F.G., P.B., R.G.

Funding acquisition: R.G.

References

- Aitken, F., Menelaou, G., Warrington, O., Koolschijn, R. S., Corbin, N., Callaghan, M. F., & Kok, P. (2020). Prior expectations evoke stimulus-specific activity in the deep layers of the primary visual cortex. *PLoS Biology*, 18(12), 1–19. <https://doi.org/10.1371/journal.pbio.3001023>
- Alkemade, A., Bazin, P. L., Balesar, R., Pine, K., Kirilina, E., Möller, H. E., Trampel, R., Kros, J. M., Keuken, M. C., Bleys, R. L., Swaab, D. F., Herrler, A., Weiskopf, N., & Forstmann, B. U. (2022). A unified 3D map of microscopic architecture and MRI of the human brain. *Science Advances*, 8(17), 1–10. <https://doi.org/10.1126/sciadv.abj7892>

- Amunts, K., Lepage, C., Borgeat, L., Mohlberg, H., Dickscheid, T., Rousseau, M. É., Bludau, S., Bazin, P. L., Lewis, L. B., Oros-Peusquens, A. M., Shah, N. J., Lippert, T., Zilles, K., & Evans, A. C. (2013). BigBrain: An ultrahigh-resolution 3D human brain model. *Science*, *340*(6139), 1472–1475. <https://doi.org/10.1126/science.1235381>
- Bandettini, P. A., Wong, E. C., Hinks, R. S., Tikofsky, R. S., & Hyde, J. S. (1992). Time course EPI during task activation. *Magnetic Resonance in Medicine*, *25*, 390–397.
- Bollmann, S., Mattern, H., Bernier, M., Robinson, S. D., Park, D., Speck, O., & Polimeni, J. R. (2022). Imaging of the pial arterial vasculature of the human brain in vivo using highresolution 7T time-of-flight angiography. *eLife*, *11*, 1–35. <https://doi.org/10.7554/eLife.71186>
- Boon, B. D., Pouwels, P. J., Jonkman, L. E., Keijzer, M. J., Preziosa, P., Van De Berg, W. D., Geurts, J. J., Scheltens, P., Barkhof, F., Rozemuller, A. J., Bouwman, F. H., & Steenwijk, M. D. (2019). Can post-mortem MRI be used as a proxy for in vivo? A case study. *Brain Communications*, *1*(1), 1–10. <https://doi.org/10.1093/braincomms/fcz030>
- Brodman, K. (1909). Vergleichende Lokalisationslehre der Großhirnrinde in ihren Prinzipien dargestellt auf Grund des Zellenbaues. *44*(0).
- De Martino, F., Yacoub, E., Kemper, V., Moerel, M., Uludag, K., De Weerd, P., Ugurbil, K., Goebel, R., & Formisano, E. (2018). The impact of ultra-high field MRI on cognitive and computational neuroimaging. *NeuroImage*, *168*(October 2016), 366–382. <https://doi.org/10.1016/j.neuroimage.2017.03.060>
- Deistung, A., Hametner, S., Endmayr, V., Wachter, J., Feng, X., Lassmann, H., Reichenbach, J., Robinson, S., Haimburger, E., Menard, C., Haider, T., Traxler, H., Trattnig, S., & Grabner, G. (2016). Tissue fixation affects the magnetic susceptibility and effective transverse relaxation rate of brain tissue. *Magnetic Resonance Materials in Physics, Biology and Medicine*, *29*(S1), 250. <http://dx.doi.org/10.1007/s10334-016-0569-9> <http://link.springer.com/10.1007/s10334-016-0569-9>
- Dinse, J., Härtwich, N., Waehnert, M. D., Tardif, C. L., Schäfer, A., Geyer, S., Preim, B., Turner, R., & Bazin, P. L. (2015). A cytoarchitecture-driven myelin model reveals area-specific signatures in human primary and secondary areas using ultra-high resolution in-vivo brain MRI. *NeuroImage*, *114*, 71–87. <https://doi.org/10.1016/j.neuroimage.2015.04.023>
- Dresbach, S., Huber, R., Gulban, O. F., Pizzuti, A., Trampel, R., Ivanov, D., Weiskopf, N., & Goebel, R. (2024a). Characterisation of laminar and vascular spatiotemporal dynamics of CBV and BOLD signals using VASO and ME-GRE at 7T in humans. *bioRxiv*, 2024.01.25.576050. <http://biorxiv.org/content/early/2024/01/26/2024.01.25.576050.abstract>
- Dresbach, S., Huber, R., Gulban, O. F., Pizzuti, A., Trampel, R., Ivanov, D., Weiskopf, N., & Goebel, R. (2024b). Characterisation of laminar and vascular spatiotemporal dynamics of CBV and

BOLD signals using VASO and ME-GRE at 7T in humans. *bioRxiv*, 2024.01.25.576050. <http://biorxiv.org/content/early/2024/01/26/2024.01.25.576050.abstract>

Feinberg, D. A., Beckett, A. J., Vu, A. T., Stockmann, J., Huber, L., Ma, S., Ahn, S., Setsompop, K., Cao, X., Park, S., Liu, C., Wald, L. L., Polimeni, J. R., Mareyam, A., Gruber, B., Stirnberg, R., Liao, C., Yacoub, E., Davids, M., . . . Dietz, P. (2023). Next-generation MRI scanner designed for ultra-high-resolution human brain imaging at 7 Tesla. *Nature Methods*, 20(12), 2048–2057. <https://doi.org/10.1038/s41592-023-02068-7>

Fischl, B., & Sereno, M. I. (2018). *Microstructural parcellation of the human brain* (Vol. 182). <https://doi.org/10.1016/j.neuroimage.2018.01.036>

Fracasso, A., Luijten, P. R., Dumoulin, S. O., & Petridou, N. (2018). Laminar imaging of positive and negative BOLD in human visual cortex at 7 T. *NeuroImage*, 164(February 2017), 100–111. <https://doi.org/10.1016/j.neuroimage.2017.02.038>

Glasser, M. F., Coalson, T. S., Robinson, E. C., Hacker, C. D., Harwell, J., Yacoub, E., Ugurbil, K., Andersson, J., Beckmann, C. F., Jenkinson, M., Smith, S. M., & Van Essen, D. C. (2016). A multi-modal parcellation of human cerebral cortex. *Nature*, 536(7615), 171–178. <https://doi.org/10.1038/nature18933>

Goebel, R. (2012). BrainVoyager - Past, present, future. *NeuroImage*, 62(2), 748–756. <https://doi.org/10.1016/j.neuroimage.2012.01.083>

Guidi, M., Huber, L., Lampe, L., Merola, A., Ihle, K., & Möller, H. E. (2020). Cortical laminar resting-state signal fluctuations scale with the hypercapnic blood oxygenation level-dependent response. *Human Brain Mapping*, 41(8), 2014–2027. <https://doi.org/10.1002/hbm.24926>

Gulban, O. F. (2024). Multi-slab whole-brain in vivo 0.35 mm human brain at 7 T to validate acceleration & denoising. <https://doi.org/10.6084/m9.figshare.26045911.v1>

Gulban, O. F., Bollmann, S., Huber, R., Wagstyl, K., Goebel, R., Poser, B. A., Kay, K., & Ivanov, D. (2022). Mesoscopic in vivo human T2* dataset acquired using quantitative MRI at 7 Tesla. *NeuroImage*, 264(July), 119733. <https://doi.org/10.1016/j.neuroimage.2022.119733>

Gulban, O. F., Schneider, M., Marquardt, I., Haast, R. A., & De Martino, F. (2018). A scalable method to improve gray matter segmentation at ultra high field MRI. *PLoS ONE*, 13(6), 1–31. <https://doi.org/10.1371/journal.pone.0198335>

Havlicek, M., & Uludağ, K. (2020). A dynamical model of the laminar BOLD response. *NeuroImage*, 204(August 2019). <https://doi.org/10.1016/j.neuroimage.2019.116209>

Huang, T., Chen, X., Jiang, J., Zhen, Z., & Liu, J. (2019). A probabilistic atlas of the human motion complex built from large-scale functional localizer data. *Human Brain Mapping*, 40(12), 3475–3487. <https://doi.org/10.1002/hbm.24610>

- Huber, L., Handwerker, D. A., Jangraw, D. C., Chen, G., Hall, A., Stüber, C., Gonzalez-Castillo, J., Ivanov, D., Marrett, S., Guidi, M., Goense, J., Poser, B. A., & Bandettini, P. A. (2017). High-Resolution CBV-fMRI Allows Mapping of Laminar Activity and Connectivity of Cortical Input and Output in Human M1. *Neuron*, 96(6), 1253–1263. <https://doi.org/10.1016/j.neuron.2017.11.005>
- Huber, L., Poser, B. A., Bandettini, P. A., Arora, K., Wagstyl, K., Cho, S., Goense, J., Nothnagel, N., Morgan, A. T., van den Hurk, J., Müller, A. K., Reynolds, R. C., Glen, D. R., Goebel, R., & Gulban, O. F. (2021). LayNii: A software suite for layer-fMRI. *NeuroImage*, 237(May), 118091. <https://doi.org/10.1016/j.neuroimage.2021.118091>
- Jonkman, L. E., Graaf, Y. G. d., Bulk, M., Kaaij, E., Pouwels, P. J., Barkhof, F., Rozemuller, A. J., van der Weerd, L., Geurts, J. J., & van de Berg, W. D. (2019). Normal Aging Brain Collection Amsterdam (NABCA): A comprehensive collection of postmortem high-field imaging, neuropathological and morphometric datasets of non-neurological controls. *NeuroImage: Clinical*, 22(September 2018), 101698. <https://doi.org/10.1016/j.nicl.2019.101698>
- Kindle, L. M., Kakadiaris, I. A., Ju, T., & Carson, J. P. (2011). A semiautomated approach for artefact removal in serial tissue cryosections. *Journal of Microscopy*, 241(2), 200–206. <https://doi.org/10.1111/j.1365-2818.2010.03424.x>
- Koopmans, P. J., & Yacoub, E. (2019). Strategies and prospects for cortical depth dependent T2 and T2* weighted BOLD fMRI studies. *NeuroImage*, 197(March), 668–676. <https://doi.org/10.1016/j.neuroimage.2019.03.024>
- Lee, J., Stile, C. L., Bice, A. R., Rosenthal, Z. P., Yan, P., Snyder, A. Z., Lee, J. M., & Bauer, A. Q. (2021). Opposed hemodynamic responses following increased excitation and parvalbumin-based inhibition. *Journal of Cerebral Blood Flow and Metabolism*, 41(4), 841–856. <https://doi.org/10.1177/0271678X20930831>
- Lüsebrink, F., Mattern, H., Yakupov, R., Acosta-Cabronero, J., Ashtarayeh, M., Oeltze-Jafra, S., & Speck, O. (2021). Comprehensive ultrahigh resolution whole brain in vivo MRI dataset as a human phantom. *Scientific Data*, 8(1), 1–13. <https://doi.org/10.1038/s41597-021-00923-w>
- Mancini, M., Casamitjana, A., Peter, L., Robinson, E., Crampsie, S., Thomas, D. L., Holton, J. L., Jaunmuktane, Z., & Iglesias, J. E. (2020). A multimodal computational pipeline for 3D histology of the human brain. *Scientific Reports*, 10(1), 1–21. <https://doi.org/10.1038/s41598-020-69163-z>
- Markram, H., Toledo-Rodriguez, M., Wang, Y., Gupta, A., Silberberg, G., & Wu, C. (2004). Interneurons of the neocortical inhibitory system. *Nature Reviews Neuroscience*, 5(10), 793–807. <https://doi.org/10.1038/nrn1519>
- Markuerkiaga, I., Barth, M., & Norris, D. G. (2016). A cortical vascular model for examining the specificity of the laminar BOLD signal. *NeuroImage*, 132, 491–498. <https://doi.org/10.1016/j.neuroimage.2016.02.073>

- 655 Markuerkiaga, I., Marques, J. P., Gallagher, T. E., & Norris, D. G. (2021). Estimation of laminar BOLD
656 activation profiles using deconvolution with a physiological point spread function. *Journal of*
657 *Neuroscience Methods*, 353(December 2020). <https://doi.org/10.1016/j.jneumeth.2021.109095>
- 658 Meyer, H. S., Schwarz, D., Wimmer, V. C., Schmitt, A. C., Kerr, J. N., Sakmann, B., & Helmstaedter, M.
659 (2011). Inhibitory interneurons in a cortical column form hot zones of inhibition in layers 2 and
660 5A. *Proceedings of the National Academy of Sciences of the United States of America*, 108(40),
661 16807–16812. <https://doi.org/10.1073/pnas.1113648108>
- 662 Moeller, S., Yacoub, E., Olman, C. A., Auerbach, E., Strupp, J., Harel, N., & Ugurbil, K. (2010).
663 Multiband multislice GE-EPI at 7 tesla, with 16-fold acceleration using partial parallel imaging
664 with application to high spatial and temporal whole-brain fMRI. *Magnetic Resonance in Medicine*,
665 63(5), 1144–1153. <https://doi.org/10.1002/mrm.22361>
- 666 Moon, H. S., Jiang, H., Vo, T. T., Jung, W. B., Vazquez, A. L., & Kim, S. G. (2021). Contribution of
667 Excitatory and Inhibitory Neuronal Activity to BOLD fMRI. *Cerebral Cortex*, 31(9), 4053–4067.
668 <https://doi.org/10.1093/cercor/bhab068>
- 669 Mourik, T. V., Koopmans, P. J., Bains, L. J., Norris, D. G., & Fm, J. (2021). Investigation of layer
670 specific BOLD during visual attention in the human visual cortex. *bioRxiv*, 1–17. <https://doi.org/10.1101/2021.02.07.430129>
- 671
- 672 Mouritzen Dam A. (1979). Shrinkage of the brain during histological procedures with fixation in formalde-
673 hyde solutions of different concentrations. *J Hirnforsch.*, 20(2), 115–119.
- 674 Nieuwenhuys, R. (2013). The myeloarchitectonic studies on the human cerebral cortex of the Vogt-Vogt
675 school, and their significance for the interpretation of functional neuroimaging data. *Brain Structure*
676 *and Function*, 218(2), 303–352. <https://doi.org/10.1007/s00429-012-0460-z>
- 677 Ogawa, S., Tank, D. W., Menon, R., Ellermann, J. M., Kim, S. G., Merkle, H., & Ugurbil, K. (1992).
678 Intrinsic signal changes accompanying sensory stimulation: Functional brain mapping with magnetic
679 resonance imaging. *Proceedings of the National Academy of Sciences of the United States of*
680 *America*, 89(13), 5951–5955. <https://doi.org/10.1073/pnas.89.13.5951>
- 681 Pais-Roldán, P., Yun, S. D., Palomero-Gallagher, N., & Shah, N. J. (2020, December). Cortical depth-
682 dependent human fMRI of resting-state networks using EPIK. [https://doi.org/10.1101/2020.12.](https://doi.org/10.1101/2020.12.07.414144)
683 07.414144
- 684 Petro, L. S., & Muckli, L. (2017). The laminar integration of sensory inputs with feedback signals in
685 human cortex. *Brain and Cognition*, 112, 54–57. <https://doi.org/10.1016/j.bandc.2016.06.007>
- 686 Pizzuti, A., Gulban, O. F., Huber, L. R., Peters, J., & Goebel, R. (2024). In the brain of the beholder :
687 bi-stable motion reveals mesoscopic-scale feedback modulation in V1.

- Pizzuti, A., Huber, L. (, Gulban, O. F., Benitez-Andonegui, A., Peters, J., & Goebel, R. (2023). Imaging the columnar functional organization of human area MT+ to axis-of-motion stimuli using VASO at 7 Tesla. *Cerebral Cortex*, 33(13), 8693–8711. <https://doi.org/10.1093/cercor/bhad151>
- Rosenke, M., Van Hoof, R., Van Den Hurk, J., Grill-Spector, K., & Goebel, R. (2021). A Probabilistic Functional Atlas of Human Occipito-Temporal Visual Cortex. *Cerebral Cortex*, 31(1), 603–619. <https://doi.org/10.1093/cercor/bhaa246>
- Rudy, B., Fishell, G., Lee, S. H., & Hjerling-Leffler, J. (2011). Three groups of interneurons account for nearly 100% of neocortical GABAergic neurons. *Developmental Neurobiology*, 71(1), 45–61. <https://doi.org/10.1002/dneu.20853>
- Schleicher, A., Amunts, K., Geyer, S., Morosan, P., & Zilles, K. (1999a). Observer-independent method for microstructural parcellation of cerebral cortex: A quantitative approach to cytoarchitectonics. *NeuroImage*, 9(1), 165–177. <https://doi.org/10.1006/nimg.1998.0385>
- Schleicher, A., Amunts, K., Geyer, S., Morosan, P., & Zilles, K. (1999b). Observer-independent method for microstructural parcellation of cerebral cortex: A quantitative approach to cytoarchitectonics. *NeuroImage*, 9(1), 165–177. <https://doi.org/10.1006/nimg.1998.0385>
- Shmuel, A., Yacoub, E., Chaimow, D., Logothetis, N. K., & Ugurbil, K. (2007). Spatio-temporal point-spread function of fMRI signal in human gray matter at 7 Tesla. *NeuroImage*, 35(2), 539–552. <https://doi.org/10.1016/j.neuroimage.2006.12.030>
- Torres-Gomez, S., Blonde, J. D., Mendoza-Halliday, D., Kuebler, E., Everest, M., Wang, X. J., Inoue, W., Poulter, M. O., & Martinez-Trujillo, J. (2020). Changes in the Proportion of Inhibitory Interneuron Types from Sensory to Executive Areas of the Primate Neocortex: Implications for the Origins of Working Memory Representations. *Cerebral Cortex*, 30(8), 4544–4562. <https://doi.org/10.1093/cercor/bhaa056>
- Trampel, R., Bazin, P. L., Pine, K., & Weiskopf, N. (2019). In-vivo magnetic resonance imaging (MRI) of laminae in the human cortex. *NeuroImage*, 197(April 2017), 707–715. <https://doi.org/10.1016/j.neuroimage.2017.09.037>
- Tremblay, R., Lee, S., & Rudy, B. (2016). GABAergic Interneurons in the Neocortex: From Cellular Properties to Circuits. *Neuron*, 91(2), 260–292. <https://doi.org/10.1016/j.neuron.2016.06.033>
- Turner, R. (2019). Myelin and modeling: Bootstrapping cortical microcircuits. *Frontiers in Neural Circuits*, 13(May), 1–11. <https://doi.org/10.3389/fncir.2019.00034>
- Tustison, N. J., Avants, B. B., Cook, P. A., Zheng, Y., Egan, A., Yushkevich, P. A., & Gee, J. C. (2010). N4ITK: Improved N3 bias correction. *IEEE Transactions on Medical Imaging*, 29(6), 1310–1320. <https://doi.org/10.1109/TMI.2010.2046908>
- Uğurbil, K., Adriany, G., Andersen, P., Chen, W., Garwood, M., Gruetter, R., Henry, P. G., Kim, S. G., Lieu, H., Tkac, I., Vaughan, T., Van De Moortele, P. F., Yacoub, E., & Zhu, X. H. (2003).

723 Ultrahigh field magnetic resonance imaging and spectroscopy. *Magnetic Resonance Imaging*,
724 21(10), 1263–1281. <https://doi.org/10.1016/j.mri.2003.08.027>

725 Uludag, K., & Havlicek, M. (2021). Determining laminar neuronal activity from BOLD fMRI using a
726 generative model. *Progress in Neurobiology*, (March), 102055. <https://doi.org/10.1016/j.pneurobio.2021.102055>

728 Uludağ, K., Müller-Bierl, B., & Uğurbil, K. (2009). An integrative model for neuronal activity-induced
729 signal changes for gradient and spin echo functional imaging. *NeuroImage*, 48(1), 150–165.
730 <https://doi.org/10.1016/J.NEUROIMAGE.2009.05.051>

731 Viessmann, O., & Polimeni, J. R. (2021). High-resolution fMRI at 7 Tesla: challenges, promises and
732 recent developments for individual-focused fMRI studies. *Current Opinion in Behavioral Sciences*,
733 40, 96–104. <https://doi.org/10.1016/j.cobeha.2021.01.011>

734 Virtanen, P., Gommers, R., Oliphant, T. E., Haberland, M., Reddy, T., Cournapeau, D., Burovski, E.,
735 Peterson, P., Weckesser, W., Bright, J., van der Walt, S. J., Brett, M., Wilson, J., Millman, K. J.,
736 Mayorov, N., Nelson, A. R., Jones, E., Kern, R., Larson, E., . . . Vázquez-Baeza, Y. (2020). SciPy
737 1.0: fundamental algorithms for scientific computing in Python. *Nature Methods*, 17(3), 261–272.
738 <https://doi.org/10.1038/s41592-019-0686-2>

739 Vizioli, L., Moeller, S., Dowdle, L., Akçakaya, M., De Martino, F., Yacoub, E., & Uğurbil, K. (2021).
740 Lowering the thermal noise barrier in functional brain mapping with magnetic resonance imaging.
741 *Nature Communications*, 12(1), 5181. <https://doi.org/10.1038/S41467-021-25431-8>

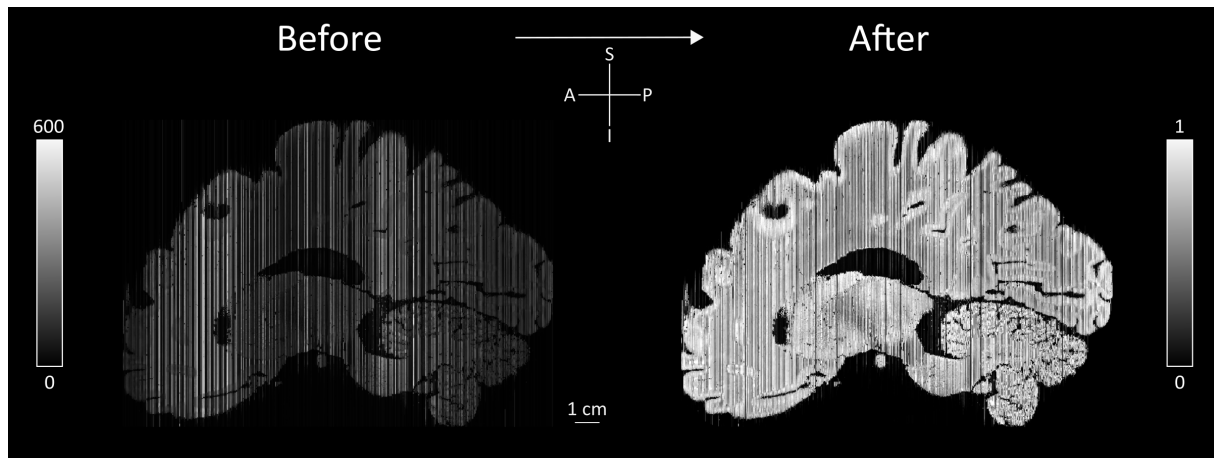
742 Vogt. (1906). Über strukturelle Hirnzentra mit besonderer Berücksichtigung der strukturellen Felder des
743 Cortex pallii. *Anat Anz*, (29), 74–114.

744 Weiskopf, N., Edwards, L. J., Helms, G., Mohammadi, S., & Kirilina, E. (2021). Quantitative magnetic
745 resonance imaging of brain anatomy and in vivo histology. *Nature Reviews Physics*, 3(8), 570–588.
746 <https://doi.org/10.1038/s42254-021-00326-1>

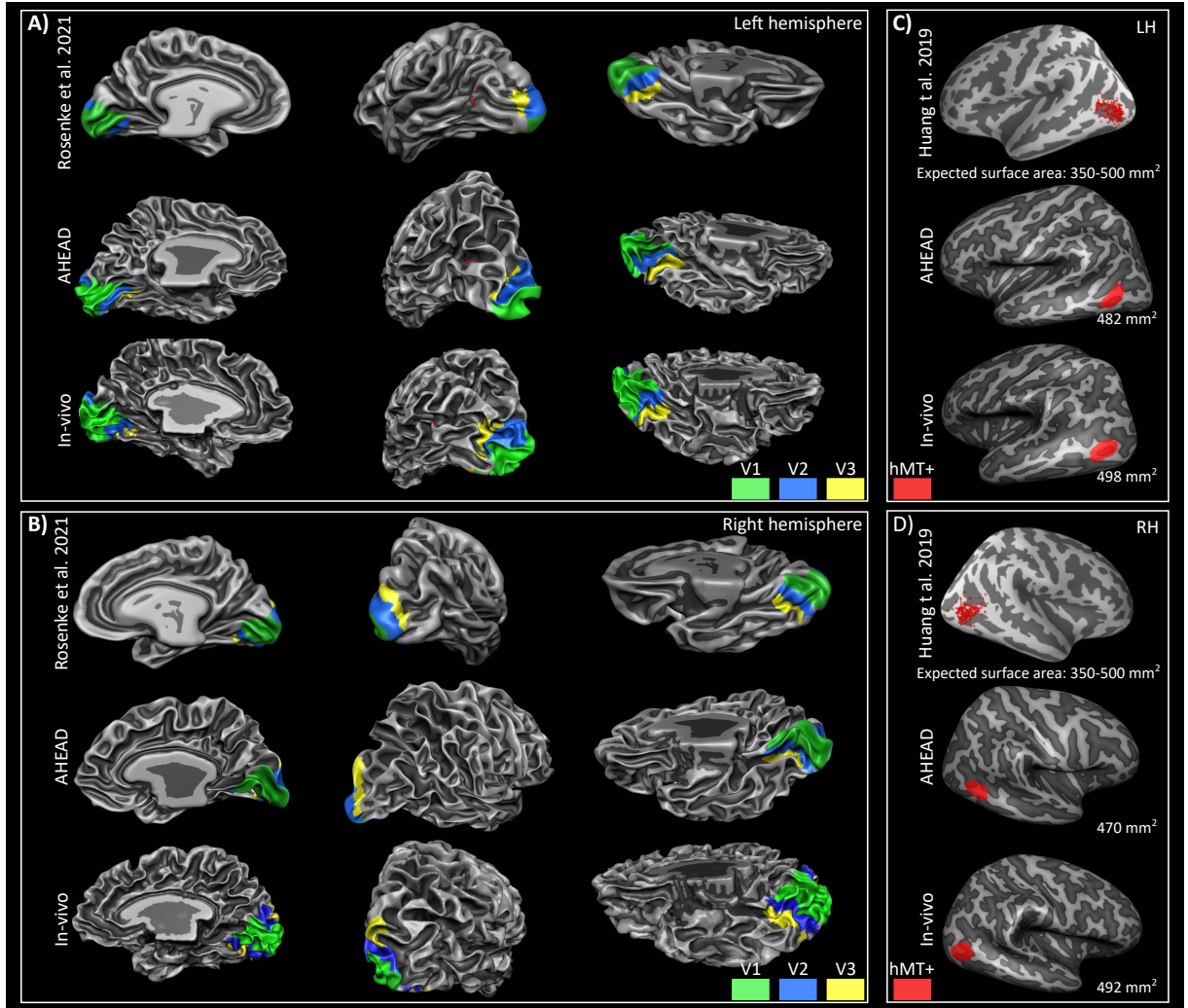
747 Yushkevich, P. A., Piven, J., Hazlett, H. C., Smith, R. G., Ho, S., Gee, J. C., & Gerig, G. (2006). User-
748 guided 3D active contour segmentation of anatomical structures: Significantly improved efficiency
749 and reliability. *NeuroImage*, 31(3), 1116–1128. <https://doi.org/10.1016/j.neuroimage.2006.01.015>

750 Zilles, K., & Amunts, K. (2010). Centenary of Brodmann’s map conception and fate. <https://doi.org/10.1038/nrn2776>

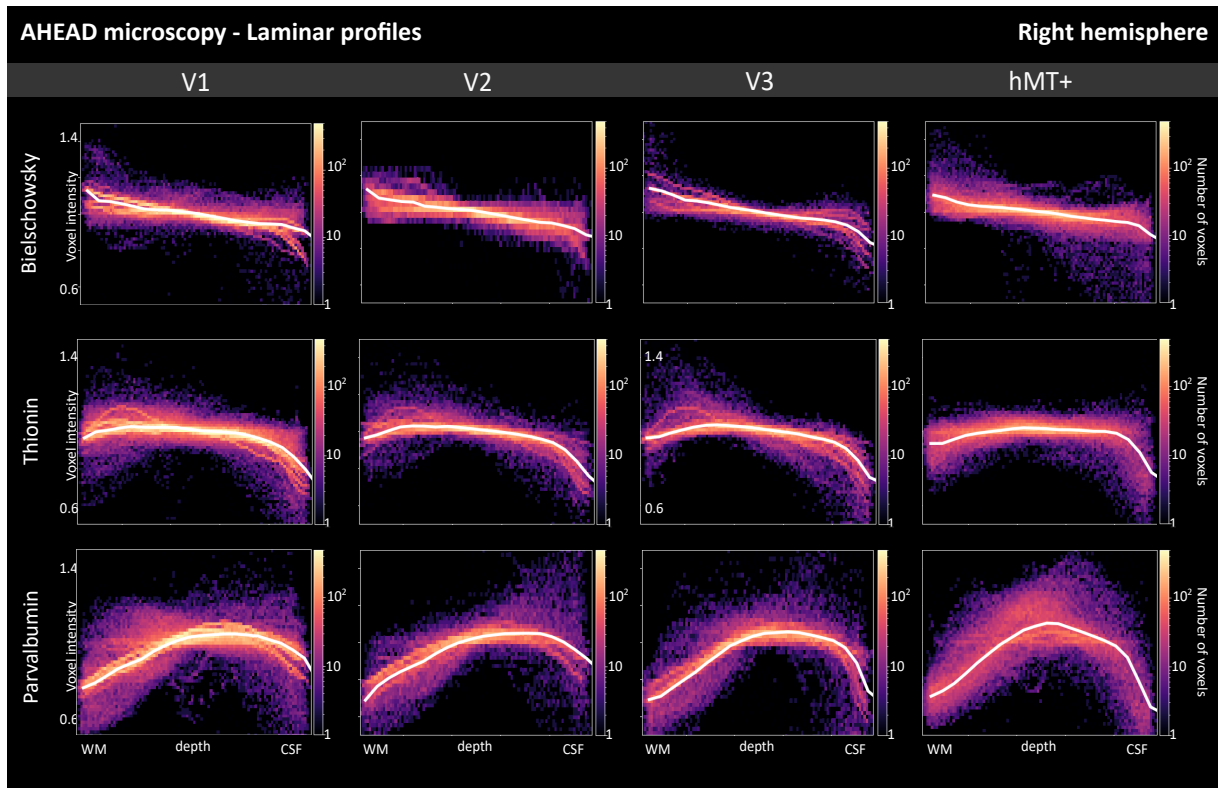
9 Supplementary Material



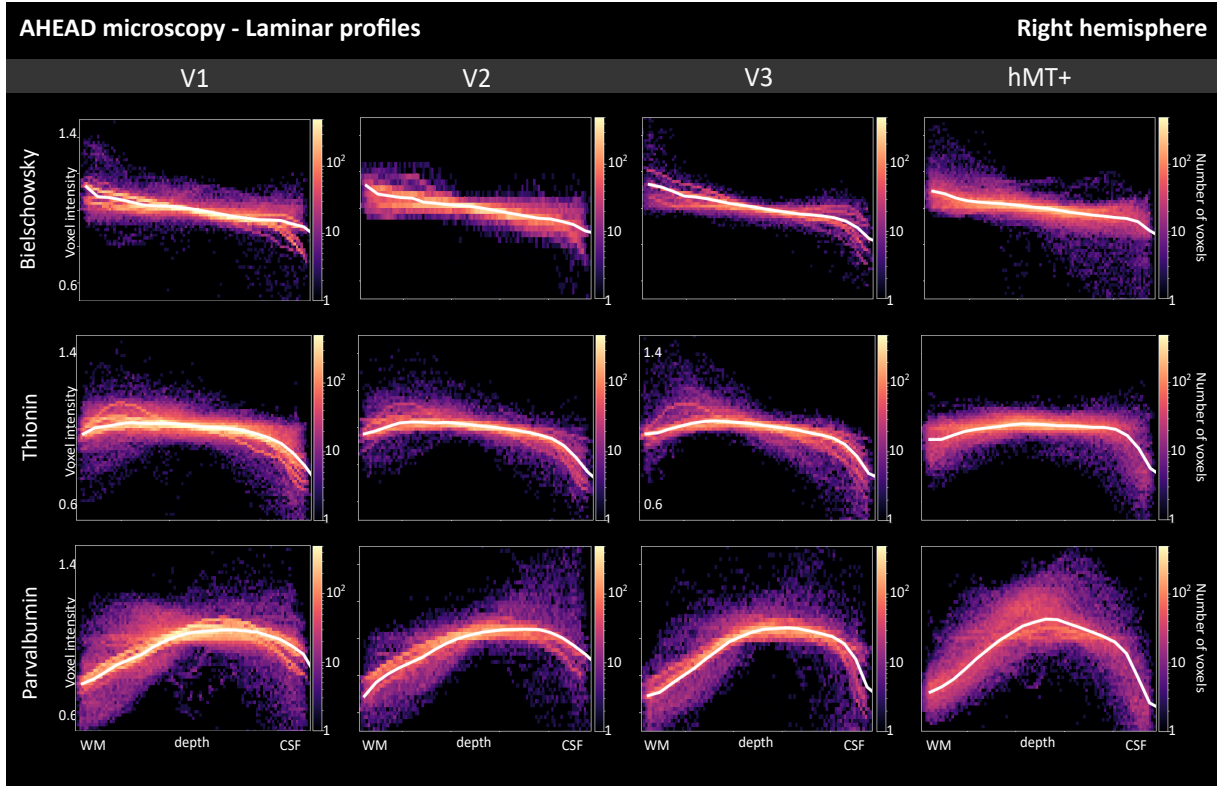
Supplementary Figure 1: Slice-based percentile intensity normalization. Comparing AHEAD stack microscopy data (sagittal view) before and after this step. The intensity of each slice is normalized between 0-1.



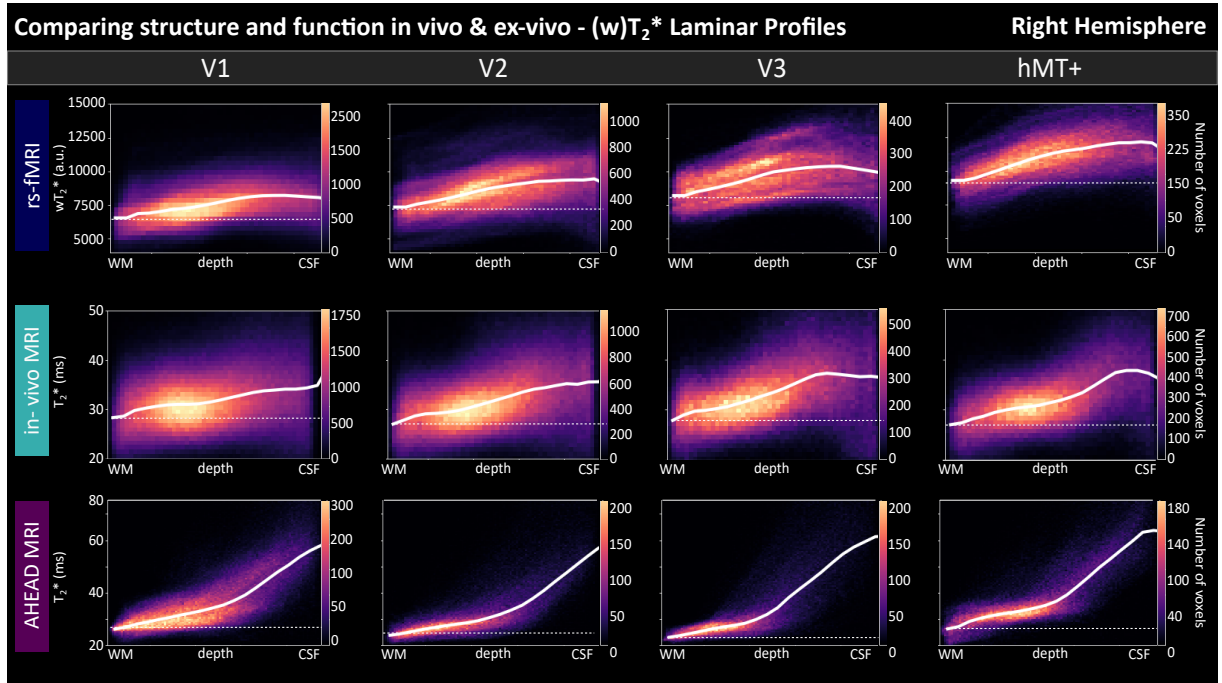
Supplementary Figure 2: Extended ROI definition for both AHEAD and In-vivo datasets. Results from cortex-based alignment to the visual functional atlas (Rosenke et al. 2021) are shown on a white matter surface for both the left (A) and the right (B) hemisphere. Results from the macro-anatomical definition of hMT+ as explained in Huang et al. 2019 are shown on the inflated white matter surface for both the left (C) and the right (D) hemisphere. Surface area is reported for each hMT+ ROIs.



Supplementary Figure 3: AHEAD laminar profiles for three microscopy contrasts (Bieloschowsky, Thionin, Parvalbumin) are shown as 2D histograms for each ROI of the right hemisphere. Gray matter cortical depth measure is shown from white matter ($x=0$) to cerebro-spinal fluid ($x=1$) boundary from left to right. Solid white lines in each subplot show median intensity for 21 discrete equivolume layers. The Y-axis is shown within the 0.5-1.4 (a.u.) range for each subplot. Results from the left hemisphere are shown in main Figure 5.



Supplementary Figure 4: AHEAD (top) and in-vivo (bottom) qR_2^* laminar profiles are shown as 2D histograms for each ROI for the right hemisphere. Gray matter cortical depth measure is shown from white matter ($x=0$) to cerebro-spinal fluid ($x=1$) boundary from left to right. Solid white lines in each subplot show median intensity for 21 discrete equivolume layers. The Y-axis is shown within the 10-50 (s-1) range for each subplot. Results from the left hemisphere are shown in main Figure 6.



Supplementary Figure 5: Structure-to-function comparison. Resting-state fMRI (top), in-vivo T_2^* (middle) and post-mortem AHEAD T_2^* (bottom) laminar profiles are shown as 2D histograms for each ROI for the right hemisphere. Gray matter cortical depth measure is shown from white matter ($x=0$) to cerebro-spinal fluid ($x=1$) boundary from left to right. Solid white lines in each subplot show median intensity for 21 discrete equivolume layers. Dotted lines indicate horizontal lines to highlight the increase towards superficial layers of main curves. The Y-axis range is displayed only in the first subplot of each data type and kept invariant across ROIs. Results from the left hemisphere are shown in main Figure 7.